Delft University of Technology

Modeling the Dynamics of the Atmospheric Boundary Layer Over the Antarctic Plateau With a General Circulation Model

Vignon, Etienne; Hourdin, Frédéric; Genthon, Christophe; Van de Wiel, Bas J.H.; Gallée, Hubert; Madeleine, Jean Baptiste; Beaumet, Julien

Important note
To cite this publication, please use the final published version (if applicable).
Please check the document version above.

Modeling the Dynamics of the Atmospheric Boundary Layer Over the Antarctic Plateau With a General Circulation Model

Etienne Vignon[1] (iD), Frédéric Hourdin[2], Christophe Genthon[1], Bas J. H. Van de Wiel[3], Hubert Gallée[1] (iD), Jean-Baptiste Madeleine[4], and Julien Beaumet[1]

[1]Univ. Grenoble Alpes, CNRS, IRD, IGE, Grenoble, France, [2]CNRS, UMR 8539, Laboratoire de Météorologie Dynamique (IPSL), Paris, France, [3]Faculty of Civil Engineering and Geosciences, Geoscience and Remote Sensing, Delft University of Technology, Delft, the Netherlands, [4]Sorbonne Universités, UPMC Univ Paris 06, UMR 8539, Laboratoire de Météorologie Dynamique (IPSL), Paris, France

Abstract Observations evidence extremely stable boundary layers (SBL) over the Antarctic Plateau and sharp regime transitions between weakly and very stable conditions. Representing such features is a challenge for climate models. This study assesses the modeling of the dynamics of the boundary layer over the Antarctic Plateau in the LMDZ general circulation model. It uses 1 year simulations with a stretched-grid over Dome C. The model is nudged with reanalyses outside of the Dome C region such as simulations can be directly compared to in situ observations. We underline the critical role of the downward longwave radiation for modeling the surface temperature. LMDZ reasonably represents the near-surface seasonal profiles of wind and temperature but strong temperature inversions are degraded by enhanced turbulent mixing formulations. Unlike ERA-Interim reanalyses, LMDZ reproduces two SBL regimes and the regime transition, with a sudden increase in the near-surface inversion with decreasing wind speed. The sharpness of the transition depends on the stability function used for calculating the surface drag coefficient. Moreover, using a refined vertical grid leads to a better reversed "S-shaped" relationship between the inversion and the wind. Sudden warming events associated to synoptic advections of warm and moist air are also well reproduced. Near-surface supersaturation with respect to ice is not allowed in LMDZ but the impact on the SBL structure is moderate. Finally, climate simulations with the free model show that the recommended configuration leads to stronger inversions and winds over the ice-sheet. However, the near-surface wind remains underestimated over the slopes of East-Antarctica.

1. Introduction

At global scale, Antarctica is a major sink for atmospheric energy. As such, it is critical to understand the atmospheric heat exchanges over the white continent in the context of global warming. The air loses energy through transfer toward the ice-sheet surface and via the emission of longwave radiation to space (Previdi et al., 2013). This climatological energy deficit is mainly compensated by a horizontal convergence of atmospheric energy transport (Genthon & Krinner, 1998; Previdi et al., 2013). The near-surface Antarctic atmosphere experienced significant changes during the last decades (Steig et al., 2009; Turner et al., 2006). In particular, the near-surface air over the Western part of Antarctica exhibits one of the major warming over the globe (Bromwich et al., 2013a), with heating rates larger than 0.5 K per decade at some places. Despite a significant warming in the end of the 20th century, the Antarctic Peninsula has been slightly cooling since 1998, reflecting the high natural variability of the climate in this region (Turner et al., 2016). East Antarctica has experienced a slight cooling trend (Nicolas & Bromwich, 2014; Smith & Polvani, 2017) particularly marked during autumn.

General circulation models (GCMs) are very powerful tools for investigating the mechanisms responsible for global or regional changes in the Earth climate. However, we can wonder to what extent they are able to correctly represent the near-surface temperature field over Antarctica. Although the models involved in the fifth Coupled Models Intercomparison Experiment (CMIP) have a realistic climatology and interannual variability in Antarctica, they fail in reproducing the near-surface temperature trends in the period 1979–2005 (Smith & Polvani, 2017) and particularly the contrast between west and east Antarctica.

King et al. (2001) noticed that the Antarctic surface climate is very sensitive to the boundary-layer heat flux parametrizations. When using turbulent diffusion coefficient formulations that sharply decrease with increasing static stability, the authors observed long-term mechanical decoupling of the surface from the atmosphere over large regions of East Antarctica in the HadAM2 GCM. However, they wonder whether "such behavior is realistic, or even desirable in a coarse-resolution model." A poor representation of the sensible heat flux over Antarctica in GCM has also been reported in King and Connolley (1997) and Cassano et al. (2001), and such a deficiency is expected to be partly responsible for a warm temperature bias over Antarctica in the ERA-Interim (hereafter ERA-I) reanalyses (Dutra et al., 2015; Freville et al., 2014) of the European Center for Medium-Range Forecasts (hereafter ECMWF). Evaluating and improving the representation of heat exchanges between the atmosphere and the ice-sheet in GCMs is therefore crucial.

GCMs and Numerical Weather Prediction models often apply formulations with enhanced turbulent mixing to optimize model scores at synoptic scales (Sandu et al., 2013) or to account for nonrepresented subgrid mixing processes like small-scale gravity waves (Steeneveld et al., 2008). However, these formulations are detrimental to the modeling of the stable boundary layers (SBL) structure (Cuxart et al., 2006; Svensson et al., 2011).

Even though global tuning strategies can degrade the structure of the SBL, Baas et al. (2017) show that climate models with a 1.5 order closure turbulent scheme (with a prognotic equation of the turbulent kinetic energy) have the required physics to represent reasonably the SBL for a wide range of mechanical forcings. Such models seem able to mimic the two-regime behavior of the SBL, with its weakly and very stable extremes and with the typical "reversed-S shape" dependency of the near-surface inversion with the wind forcing at Cabauw, the Netherlands (van de Wiel et al., 2017). Such a behavior is evidenced by observation in Van Hooijdonk et al. (2015), Monahan et al. (2015), and van der Linden et al. (2017). The theoretical background behind this behavior was demonstrated by van de Wiel et al. (2017). They show that the sudden regime transition can be understood in terms of the Minimum Wind speed for Sustainable Turbulence (MWST) theory (van de Wiel et al., 2012; Van Hooijdonk et al., 2015, 2017). If the wind speed is less than this minimum, the sensible heat flux is unable to compensate for the energy loss of the surface, which causes the near-surface inversion to increase rapidly. As the turbulence shuts down, the atmosphere becomes mechanically decoupled from the surface (Derbyshire, 1999) and the near-surface temperature inversion is only governed by the radiative "coupling" to the air, and the diffusive "coupling" to the soil.

Vignon et al. (2017a) evidenced that the prevailing SBL over Dome C, East Antarctic Plateau, also presents a clear two-regime behavior with a sharp transition that occurs in a narrow 10 m wind speed range. On one hand, a weakly stable regime occurs under moderate wind and/or cloudy conditions with a significant amount of turbulence and weak near-surface temperature inversions. On the other hand, a very stable regime occurs under weak wind and clear-sky conditions with weak turbulence. In this case, the near-surface temperature inversion may reach values up to 25 K between 10 m and the surface, as the coupling between the air and the snow is (essentially) of radiative origin. Riordan (1977) (see also Hudson and Brandt, 2005) and Cassano et al. (2016) (see also Wille et al., 2016) identified similar wind speed thresholds that distinguish a SBL regime with strong near-surface inversions from a regime with weak near-surface inversions at the South Pole and over the Ross ice-shelf, respectively. This suggests that the two-regime behavior of the SBL may prevail over a large part of the Antarctic continent where the surface slope is weak (ice-shelves, Plateau). In addition, the surface-atmosphere mechanical decoupling in the weak wind speed regime is critical regarding snow accumulation issues. Indeed, Berkelhammer et al. (2016) evidenced that under very stable conditions over the Greenland ice-sheet, the snow surface can be mechanically insulated from transiting tropospheric air masses, impeding both accumulation associated with surface condensation and mass loss through sublimation. After the conclusions of Vignon et al. (2017a) and van de Wiel et al. (2017), it is thus clear that not only the two-regime behavior but also long-term decouplings are realistic and climatological features of the SBL over Dome C (and likely over a wide part of Antarctica) that need to be represented in GCMs.

Beyond the Antarctic climate issue, correct modeling of the SBL dynamics is important for assessing the response of the nocturnal near-surface temperature over continents to changes in greenhouse gases concentrations (McNider et al., 2012; Walters et al., 2007) and for representing the evolution of Arctic near-surface temperatures with global warming, since a transition from a very stable to weakly stable regime would mean a transition between a state in which the warming signal remains confined in the low stratified layer to a state in which the warming is diluted to higher levels (Bintanja et al., 2012). The present study explores the ability of the Laboratoire de Météorologie Dynamique Zoom (LMDZ) GCM, the atmospheric

component of the IPSL Earth System model (Dufresne et al., 2013), to represent the dynamics of the atmospheric boundary layer over the Antarctic Plateau. In particular, it investigates how well the model represents the competition between mechanical (turbulent) and radiative surface couplings at Dome C. Beyond the evaluation of the model, simulations also give insights into the boundary-layer dynamics over the Antarctic Plateau. Our work builds on the previous evaluation of LMDZ at Dome C in Vignon et al. (2017b). The latter paper focused on the representation of a typical clear-sky summertime diurnal cycle using the 1-D version of LMDZ assessing the sensitivity to surface parameters and turbulence parametrizations. The present study extends toward the representation of a full seasonal cycle, including the polar night, and using the standard 3-D version of the model, i.e., with its intrinsic constraints on the length of the physical time step, on the model's grid and on the global-scale tuning strategy (Hourdin et al., 2017). The 3-D simulations also enable to assess how the specific improvements made to fit observations at Dome C affect the continental-scale near-surface climate. Last but not least, the present work contributed to the setup of a new version of LMDZ for the CMIP6 experiments and it will be shown that LMDZ has now consistent physical parametrizations for the extreme Antarctic SBL and reasonable surface parameters over ice-sheets. The paper is structured as follows. Section 2 presents the LMDZ model, the specific "stretched-grid and nudged" configuration of the simulations and the observations. The ability of LMDZ to represent the Dome C boundary layer is analyzed in sections 3. Section 4 discusses the representation of the near-surface Antarctic climate using standard climate simulations without nudging. Section 5 draws our conclusions.

2. Climatological Settings, Data, and Simulations

2.1. Dome C Geographical and Climatological Settings and In Situ Data

Dome C is located in the eastern part of the high Antarctic Plateau (75°06′S, 123°20′E, 3233 m a.s.l, Local Time LT = UTC + 8) where the French-Italian station Concordia has been set-up. The landscape consists in a homogeneous and flat snow desert covered by snow-eroded forms called sastrugi. The sky is predominantly clear. The air is very cold and dry, with monthly mean 2 m temperatures that range from about $-27°C$ in austral summer to about $-65°C$ in the polar night in winter (Genthon et al., 2013). The annual snow accumulation is less than 8×10^{-2} m yr^{-1} (Genthon et al., 2015). The "flatness" of the Dome prevents local generation of katabatic winds. The near-surface wind is mostly south-southwesterly (Aristidi et al., 2005) and the annual 3 m mean speed is moderate, 4.5 m s^{-1}, and rare peaks reach 12 m s^{-1} (Argentini et al., 2014). Occurrences of significant wind-transported snow events are seldom (Libois et al., 2014).

The Dome C boundary layer shows a marked seasonality. In summer (December–January), even though the sun remains always above the horizon, the boundary layer evolves with a clear diurnal cycle (Genthon et al., 2010). During the summer "day" (i.e., when the sun is high above the horizon), the boundary layer is convective and 100–300 m deep (Casasanta et al., 2014). During the summer "night" (i.e., when the sun is close to the horizon), the nocturnal SBL is shallower than 50 m and an inertial low-level jet develops (Gallée et al., 2015). During the polar night, the boundary layer is almost permanently stably stratified (Genthon et al., 2013) and the turbulent boundary layer, when present, is only a few meters or dozens of meters deep (Petenko et al., 2014; Pietroni et al., 2012). Dome C frequently experiences sudden "warming events," when warm and moist air is advected from the coast over the Plateau resulting in a large anomaly of downward long wave radiative flux and in an abrupt warming of the low troposphere of several tens of Kelvin in a few hours (Gallée & Gorodetskaya, 2010; Genthon et al., 2013).

In the present study, we use in situ data from meteorological measurements that are performed at Concordia. We use temperature and wind data obtained along a 45 m tower (Genthon et al., 2010, 2013) and a 2.5 m mast (Vignon et al., 2016) and radiation data obtained by the Baseline Surface Radiation Network (BSRN, Lanconelli et al., 2011). Details on how all of these data are processed are given in Genthon et al. (2013) and Vignon et al. (2016). Note that the surface temperature is estimated from surface longwave radiative fluxes assuming a snow emissivity of 0.99.

Genthon et al. (2017) show that classical near-surface moisture measurements are biased at Dome C since standard thermohygrometers are not capable to measure supersaturations with respect to ice because the excess moisture with respect to saturation tends to condense on the surfaces of the sampling device. Data from an innovative hygrometer installed at 3 m above the ground (so called "HMPmod" in Genthon et al., 2017) that allows for the measurement of near-surface supersaturation have been used. To obtain

estimations of the integrated water vapor (IWV) in the atmospheric column above Dome C, we use hourly averaged measurements performed by an in situ H_2O Antarctica Microwave Stratospheric and Tropospheric Radiometer (HAMSTRAD) instrument (Ricaud et al., 2012, 2015). IWV as well as tropospheric profiles of temperature, humidity, and wind are also retrieved from daily Vaisala RS92 radiosoundings, launched at 2000 LT from the Routine Meteorological Observation program (http://www.climantartide.it/). Following Tomasi et al. (2006), the IWV from radiosondes is calculated from the ground to 10,000 m height. No correction for typical biases (due, for instance, to sensor aging, time lags or chemical contamination, see Tomasi et al., 2011) of temperature and humidity measurements was required because the latter biases do not significantly affect the estimation of the IWV (Ricaud et al., 2017).

2.2. The LMDZ GCM

LMDZ is the atmospheric component of the IPSL Earth-System Model used for climate studies and climate change projections, particularly in the CMIP experiments (Hourdin et al., 2013). LMDZ was particularly used for Antarctic purposes in studies on surface mass balance issues (e.g., Agosta et al., 2013; Krinner et al., 2007), on oceanic forcing on the Antarctic climate (Krinner et al., 2014) and on the transport of chemical species at high southern latitudes (Cosme et al., 2005). We used here a "pre-CMIP6" version of the model, i.e., an advanced version of LMDZ-5B (Hourdin et al., 2013).

2.2.1. Configurations of the Simulations

The simulations are conducted with the zooming capability of the model in a nudged mode, as described in Coindreau et al. (2007). The "zoom" consists in stretching the horizontal Arakawa-C 64 × 64 grid in both latitude and longitude in order to obtain a refined domain of 400 km×400 km centered on Dome C with a middle grid cell of 25 km×25 km. The grid retained here is plotted in Figure 1. In the vertical, we use the default 79 hybrid-pressure levels setup for the 6th CMIP experiment. Above Dome C, the vertical grid has 15 levels in the first 500 m of which 3 in the first 45 m (height of the meteorological tower). The first model level height varies between 5.2 m in winter and 6.8 m in summer. Likewise, the second (respectively, third) model level height varies between 17 m (respectively, 31 m) and 22 m (respectively, 39 m). As the SBL above the Antarctic Plateau may be very shallow, we also perform simulations with a refined 103 hybrid-pressure levels grid. This latter has a better resolution in the first meters above ground, with a first model level at approximately 1.5 m and with 11 levels in the first 100 m.

The model is nudged by the ECMWF ERA-I reanalyses by adding a relaxation term to the prognostic equation for four state variables:

$$\frac{\partial X}{\partial t} = F(X) - \frac{X - X^a}{\tau} \tag{1}$$

where X is the zonal and meridional wind u and v, the temperature T, and the specific humidity q_v. F is the operator describing the dynamical and physical processes that determine the evolution of X. X^a is the reanalyzed field from ERA-I interpolated on the model grid and at each model time step. τ is a relaxation time. Genthon et al. (2013) show that the synoptic evolution in the bulk of the atmosphere and the tropospheric variability are relatively well reproduced by ECMWF analyses. Different values of τ are used inside and outside the "zoomed" region with a smooth transition between the inner and outer regions that follows the grid cell size. Outside the zoom, we set $\tau^{out} = 3\,h$ and inside the zoom, $\tau^{in} = 240\,h$. A large value of τ (weak nudging) in the zoomed area enables the meteorological fields in this region to be governed by the internal physics of LMDZ rather than by the (external) reanalysis field. Such a nudging enables both an evaluation of the subcomponents of the physics of the model apart from likely deficiencies in representing the atmospheric synoptic conditions (Appendix A) and a chronologic comparison with in situ data from the Dome C observatory. The 3-D zoomed-nudged simulations start in December 2014 and they are run until 31 December 2015. The model has sufficient time to reach an atmospheric equilibrium over the Antarctic Plateau before 1 January 2015, date from which we analyze the results.

In section 4, we discuss meteorological fields not only over Dome C but over the whole Antarctic continent. For this purpose, we analyze free (i.e., without nudging) simulations performed with the standard (no "zoom") 144×142×79 grid and run over the period 2001–2011. Over continents, LMDZ is coupled with the land-surface model ORCHIDEE (Hourdin et al., 2013; Krinner et al., 2005). Sea ice cover and sea surface temperature fields are prescribed every month with climatological fields.
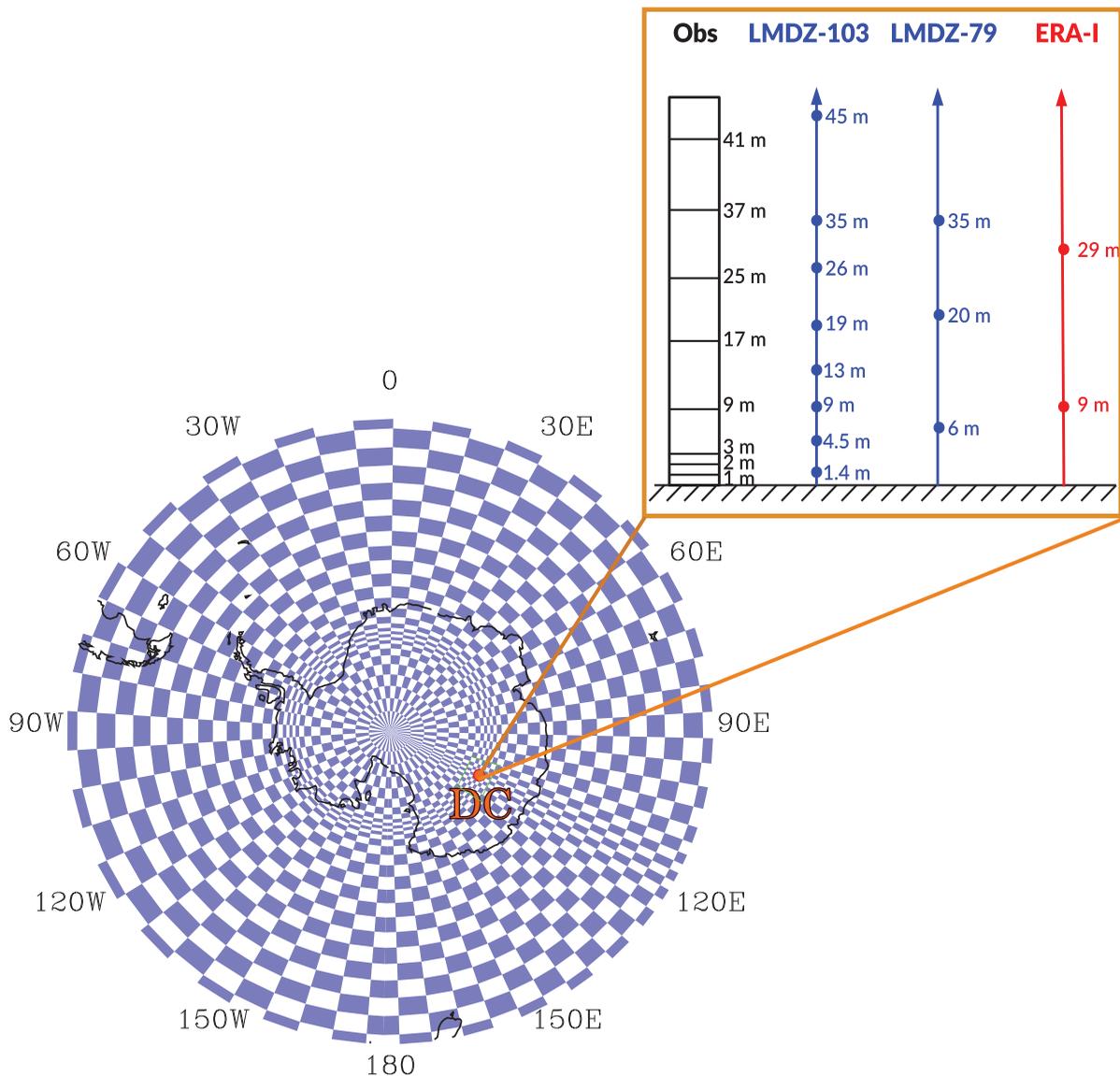
Figure 1. Polar stereographic view of the stretched-grid used for the 3-D nudged simulations. The orange dot locates Dome C (DC). In the inset are shown the approximative heights of the observation levels at Dome C and the yearly averaged heights of the vertical model levels of LMDZ and ERA-I.

2.2.2. Modifications of Physical Parametrizations

The ability of LMDZ in modeling the summertime atmospheric boundary layer at Dome C was assessed and improved by Vignon et al. (2017b) using the single column version of LMDZ on the 4th Gewex Atmospheric Boundary Layer (GABLS) case (Bazile et al., 2014, 2015). This study led to changes of the values of model's parameters over the ice-sheets:

1. The snow albedo is set to 0.96 for the visible range and to 0.68 for the near infra-red range (Grenfell & Warren, 1994) instead of 0.77 for both ranges. This low value was tuned in the CMIP3 version to compensate for a deficit of longwave downward radiation at surface.
2. The roughness lengths for momentum z_0 and for heat z_{0t} are set to 10^{-3} and 10^{-4} m, respectively. These values are close to measurements at Dome C (Vignon et al., 2016) and in reasonable agreement with measurements over other regions of the Antarctic Plateau (Amory et al., 2017).
3. The snow thermal inertia is set to 350 $J\,m^{-2}\,K^{-1}\,s^{-1/2}$ instead of the original largely overestimated value of $2,000$ $J\,m^{-2}\,K^{-1}\,s^{-1/2}$.

The parametrization of the vertical turbulent transport in the current version of LMDZ is a 1.5 order turbulence closure K-gradient scheme based on Yamada (1983). This local turbulent scheme is combined with a mass-flux scheme, the so-called "thermal plume model," for convective boundary layers (Hourdin et al., 2002; Rio et al., 2010). In stable conditions, the turbulent mixing coefficients for momentum (subscript "m") and for heat (subscript "h") read:

$$K_{m,h} = l S_{m,h} \sqrt{2 \text{TKE}} \tag{2}$$

where l is a mixing length, TKE is the turbulent kinetic energy, and $S_{m,h}$ are monotically decreasing functions of the Richardson number R_i (see Yamada, 1983). In previous versions of LMDZ, l was lower-bounded by a minimum value $l_{min} = 1$ m and $S_{m,h}$ were also lower-bounded by values $S_{m,h}(R_{ic})$, R_{ic} being a critical Richardson number equal to 0.143. Vignon et al. (2017b) pointed out that the representation of the summertime nocturnal SBL at Dome C was significantly improved when the lower-bounds of $S_{m,h}$ and l are removed. Roughly speaking, removing such thresholds enables the turbulent mixing to collapse in very stable conditions leading to more realistic shallow and very stratified SBL. In what follows, the simulations with the enhanced mixing configuration will be referred to as "minmix." In all the other simulations, $l_{min} = 0$ and $R_{ic} = 0.18$. It is worth noting that in this latter "weak mixing" configuration, the original numerical resolution of the prognostic equation of the TKE (Hourdin, 1992) does not converge at long time steps as those used for physical parametrizations in 3-D simulations (900 s for CMIP6). In fact, besides its role of mixing enhancement, the minimum mixing length was acting as a numerical artifice that helped numerical convergence in previous versions of the model. The numerical scheme has thus been changed to one proposed by Deleersnijder (1992) with better convergence properties.

The surface drag coefficient for momentum C_d and for heat and moisture C_h are computed as:

$$C_d = \frac{\kappa^2}{\ln{(z_1/z_0)}^2} \times f_m \tag{3}$$

$$C_h = \frac{\kappa^2}{\ln{(z_1/z_0)}\ln{(z_1/z_{0t})}} \times f_h \tag{4}$$

where κ is the Von Kármán constant, z_1 is the height of the first model level, z_0 and z_{0t} are the roughness lengths for momentum and heat, respectively, and f_m and f_h are functions of the local R_i between the first model level and the surface. Vignon et al. (2017b) pointed out that $f_{m,h}$ functions from (Louis et al., 1982) (hereafter L82) are significantly overestimated in stable conditions compared to in situ data over an extended summer period at Dome C. L82 functions were historically implemented to prevent surface-atmosphere decouplings over lands in 3-D simulations. We test here two additional types of function: the so-called "SHARP" functions from King et al. (2001) (hereafter K01) and so-called "cutoff" functions (England and McNider, 1995; King & Connolley, 1997), derived from the Monin-Obukhov similarity theory. These two latter types of functions decrease more sharply with R_i and the cutoff functions reach zero at $R_i = 0.2$ (see Figure 2).

In the previous versions of LMDZ, the standard radiative scheme was the one developed by Morcrette (1991) (hereafter M91) for the ECMWF. The longwave spectrum part is a six band scheme with the following radiative active species: H_2O, O_3, CO_2, N_2O, CH_4, and chlorofluorocarbons. During the setting of the CMIP6 version of LMDZ, the k-correlated Rapid Radiative Transfer Model (RRTM, Mlawer et al., 1997) was implemented for the longwave spectrum. It is now used as the standard radiative scheme. It is worth noting that RRTM is also used in several GCMs like the Weather Research and Forecasting model (Skamarock et al., 2008), in the ECMWF model (Morcrette et al., 2001) or the NCAR community climate model (Iacono et al., 2000) for instance. The main differences with the M91 are (Morcrette et al., 2001):

1. RRTM considers 16 different spectral bands, improving the spectral description of air and cloud radiative properties.
2. RRTM allows for more accurate absorption in the water-vapor continuum.

3. Representing the Boundary-Layer Dynamics at Dome C

In this section, the representation of the boundary layer at Dome C in nudged and stretched-grid LMDZ simulations is evaluated using in situ data. The analyzed simulations are listed according to their characteristics in Table 1.
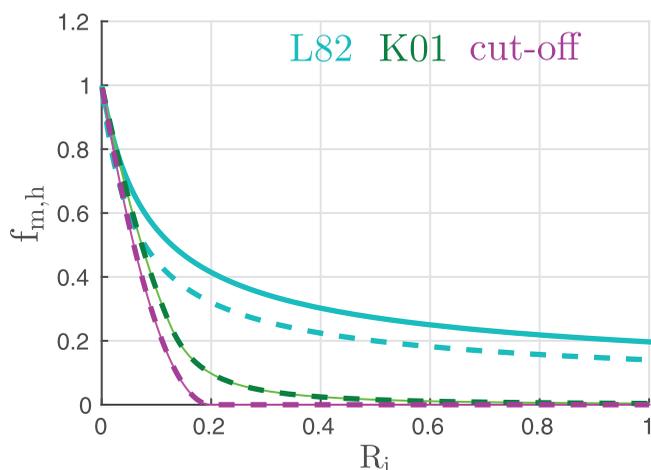
Figure 2. Stability function models used for the calculation of the surface drag coefficients versus R_i. Solid (respectively, dashed) lines show the stability function for momentum f_m (respectively, for heat f_h).

3.1. Downward Longwave Fluxes and Surface Temperatures

Modeling studies like Cerni and Parish (1984), Bromwich et al. (2013b), or Sterk et al. (2013) highlighted the sensitivity of meteorological models to the radiation scheme in polar regions, particularly in low wind conditions. Gallée and Gorodetskaya (2010) also pointed out that the main energy source term of the surface energy balance at Dome C in winter is the LW_{dn} flux. Figure 3a shows that the LW_{dn} flux in the simulation using the M91 scheme (M91-L82-79) is significantly underestimated (mean bias of -12.82 W m^{-2}). The implementation of RRTM has led to a significant improvement of the LW_{dn} flux in the RRTM-L82-79 simulation. This result is weakly sensitive to the turbulent mixing parametrization (not shown). Morcrette et al. (2001) noticed that in the ECMWF model, one of the main consequence of the introduction of RRTM in place of M91 was a significant reduction of the LW_{dn} bias at the surface over the dry and cold atmosphere like at the South Pole (Wild et al., 2001). Gallée and Gorodetskaya (2010) also noticed the improvement of the LW_{dn} simulation during the polar night at Dome C with the regional model MAR using RRTM, compared to simulations with M91. Our results agree with these conclusions.

Figure 3b shows that the relative difference in LW_{dn} between the simulation with M91 and the simulation with RRTM is maximum when the atmospheric column above Dome C is dry, i.e., at low values of the IWV. Differences are also larger when the ice water path (integrated ice content, IIC) is high. Note that IWV and IIC are very similar in M91-L82-79 and RRTM-L82-79. As such, the difference in LW_{dn} between the two simulations seems to be primarily due to the radiative scheme itself and the sensitivity to the radiative scheme is the highest when the atmosphere is dry (low IWV) and/or contains a significant amount of ice-particles (high IIC). However, the LW_{dn} in the RRTM-L82-79 simulation still show a Root Mean Square Error (RMSE) with respect to observations of 12.97 W m^{-2} over 2015. Differences in LW_{dn} with observations are mostly positive for $LW_{dn} < 100$ W m^{-2}, while they are mostly negative for $LW_{dn} > 140$ W m^{-2}. This could suggest that even RRTM struggles in representing the longwave transfer in clear-sky conditions ($LW_{dn} < 100$ W m^{-2}) or that the quantities of hydrometeors could be overestimated in cold and dry conditions at Dome C. Gallée and Gorodetskaya (2010) point out that the modeling of the LW_{dn} at Dome C is very sensitive to small variations in the water vapor content and to the modeling of thin clouds in both the troposphere and stratosphere. In fact, the cold polar atmosphere is very dry. The far infrared range, often considered as opaque at midlatitudes and low latitudes, becomes more transparent and the transmittance is thus very sensitive to the water vapor content (Palchetti et al., 2015). Moreover, clouds above the Antarctic

Table 1
Overview of the 3-D Stretched-Grid-Nudged Simulations

Simulation name	Res	l_{min} (m), R_{ic}	Surface layer	LW scheme
M91-L82-79	79	0, 0.18	L82	M91
RRTM-L82-79	79	0, 0.18	L82	RRTM
RRTM-K01–79	79	0, 0.18	K01	RRTM
RRTM-cutoff-79	79	0, 0.18	cutoff	RRTM
RRTM-minmix-L82-79	79	1, 0.143	cutoff	RRTM
RRTM-L82–103	103	0, 0.18	L82	RRTM
RRTM-K01–103	103	0, 0.18	K01	RRTM
RRTM-cutoff-103	103	0, 0.18	cutoff	RRTM
RRTM-minmix-L82–103	103	1, 0.143	cutoff	RRTM

Note. "Res" refers to the vertical resolution, "Surface layer" to the type of stability function of the drag coefficient in stable conditions and "LW scheme" to the type of radiative transfer code in the longwave spectrum. "K01" refers to King et al. (2001), "L82" to Louis et al. (1982).
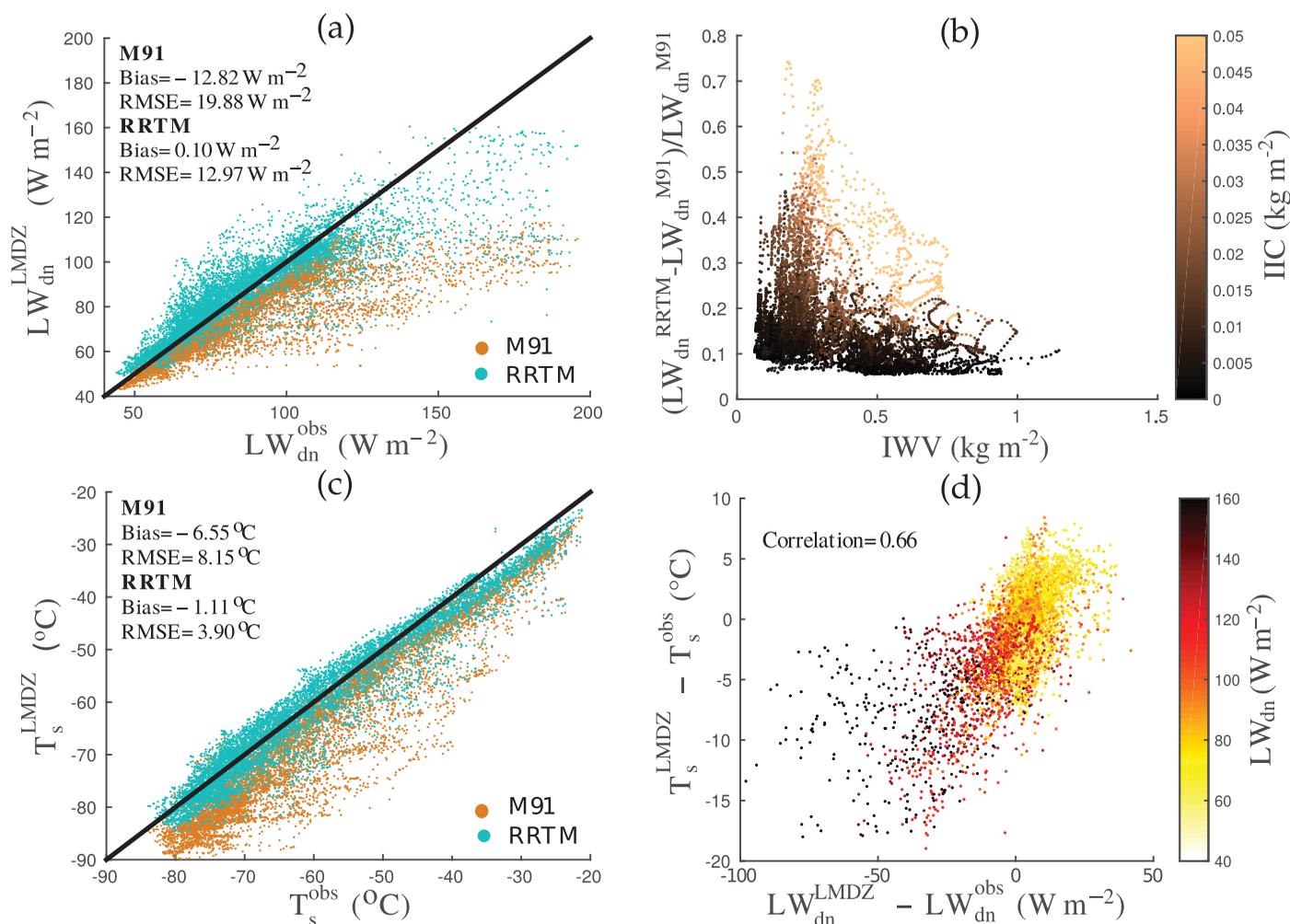
Figure 3. (a) Scatter plots of LW_{dn} at the surface in LMDZ simulations (M91-L82-79 and RRTM-L82-79) versus BSRN observations. Blue (orange) color refers to the simulation with the RRTM (M91) radiative scheme. The black line is the first bissector. (b) Relative difference of the LW_{dn} in the RRTM-L82-79 with that in the M91-L82-79 simulation versus the Integrated Water Vapor (IWV) in the atmospheric column above Dome C in the M91-L82-79 simulation. Colors show the value of the Integrated Ice Content (IIC). (c) Same as (a) but for T_s.(d): Difference of simulated (RRTM-L82-79 simulation) and observed T_s versus the difference of simulated and observed LW_{dn}. All hourly mean data in 2015 are plotted.

Plateau are rather thin, so an additional small amount of hydrometeors or a slight change in their properties (sedimentation velocities for instance) may have significant impacts on the LW_{dn} flux.

In addition, further investigation reveals that the most negative differences of LW_{dn} in the RRTM-L82-79 simulation with respect to observations coincide with peaks of IWV corresponding to northerly advections of warm and moist oceanic air, often associated to thick cloud episodes above Dome C (Ricaud et al., 2017). The amplitude of these large peaks of IWV is underestimated in our simulations (see Appendix A) and in the ERA-I reanalyses (not shown) suggesting that a part of the negative bias in LW_{dn} could be related to deficiencies in the moisture nudging by ERA-I.

As the LW_{dn} flux is the major source term in the surface energy balance during a large part of the year, the improvement of the LW_{dn} flux associated to the introduction of RRTM leads to a much better representation of the surface temperature T_s (Figure 3c). However, the surface temperature remains slightly cold-biased by 1.11°C on average over 2015 and remaining hourly T_s biases are relatively well correlated with LW_{dn} biases (Figure 3d), especially during the polar night (not shown). The present section thus highlights that a correct representation of the longwave transfer in the atmosphere is paramount to the modeling of the surface temperature at Dome C, in agreement with Bromwich et al. (2013b).

3.2. Seasonality of the Near-Surface Temperature and Wind

As using RRTM leads to better comparison with in situ measurements of radiative fluxes compared to M91, we now evaluate the seasonality of the boundary-layer temperature and wind in simulations with the RRTM radiative scheme. Figure 4a shows the annual time series of the monthly mean surface temperature T_s in LMDZ simulations (colored lines) and in observations (black line). T_s in RRTM-L82-79, RRTM-K01–79, and RRTM-cutoff-79 are close because the Richardson number in the surface layer is often <0.1, i.e., in a range in which $f_{m,h}$ stability functions do not significantly diverge. The monthly mean bias (plot b) and the monthly RMSE (plot c) are thus similar for these three simulations. In particular, the three simulations are cold-biased between May and September, with a mean bias exceeding (in negative values) −2°C in July and August (plot b). The RRTM-cutoff-79 (purple line) is the coldest simulation, in agreement with the collapse of the sensible heat flux in very stable conditions using the "cutoff" functions in the surface layer. As expected, the RRTM-minmix-L82-79 simulation (dark blue line) with enhanced mixing of heat in the SBL is significantly warmer than the other simulations and than observations during most of the year. Its monthly RMSE (dark blue line in plot c) is close to that of the other simulations from January to August, and higher by 1–1.8°C between September and November.

Figure 5 shows the composite vertical profiles of temperature and wind speed over the first 50 m above the surface for three classes. Left plots show the mean summertime (December–January, "DJ") profiles at 1400 LT and middle plots show the mean DJ profiles at 0200 LT. Note that in DJ 2015, all the observed hourly profiles at 1400 LT (respectively, 0200 LT) correspond to convective (respectively, stable) conditions. Right plots show the mean profiles during winter (June–July–August, "JJA"). Figure 5 can be analyzed in parallel with Figure 6 that shows the vertical profiles of the RMSE of LMDZ simulations with respect to observations for
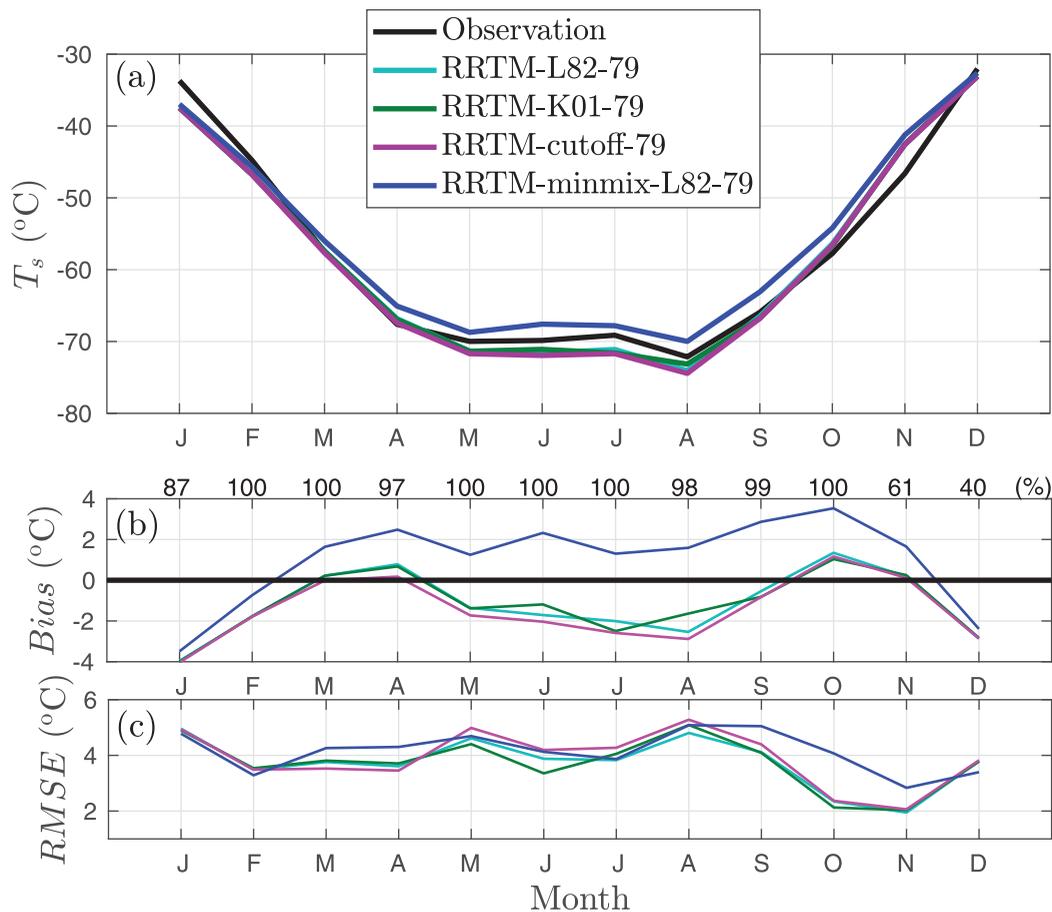
Figure 4. (a) 2015 monthly mean T_s in observations and LMDZ simulations. (b) Monthly mean bias of the simulated T_s with respect to observations. In this plot, the thick horizontal black line is the zero line. Numbers above the plot indicate the percentage of valid in situ T_s data used to compare with simulations within each month. (c) Monthly Root Mean Square Error (RMSE) of the simulated T_s in LMDZ simulations with respect to observations.
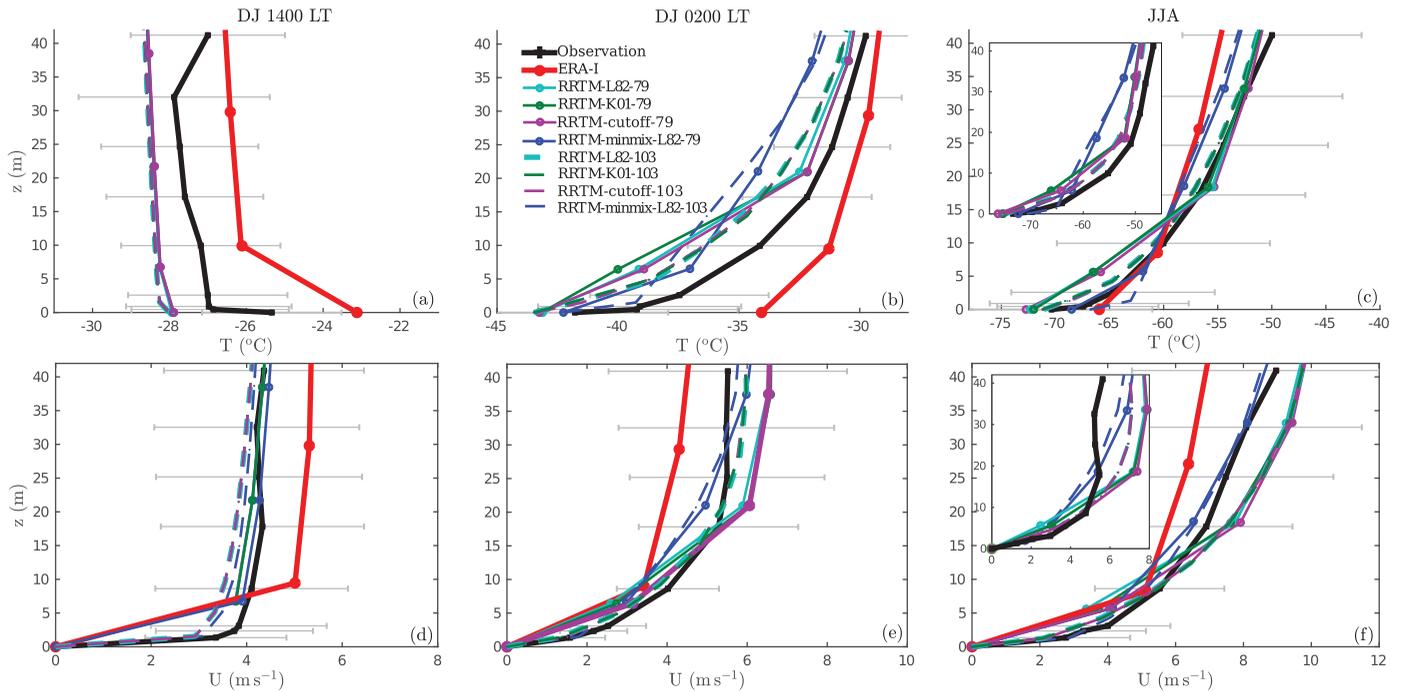
Figure 5. 2015 near-surface vertical profiles of temperature (top plots) and wind speed (bottom plots) in observations (black) and LMDZ simulations (colors). Three composites are shown. Plots a and d show the mean profiles for December–January (DJ) at 1400 LT. Plots b and e show mean profiles for DJ at 0200 LT and plots c and f show the mean profiles for June–July–August (JJA). Errorbars show the variability (±one standard deviation) in the observations for each class. As the height of model levels varies with time, the hourly vertical profiles within each composite have been first linearly interpolated in the vertical on a grid whose heights are the composite-averages of the model level heights. Then, the interpolated profiles have been averaged to obtain the composite profiles. In the insets in plots c and f are plotted the mean JJA profiles restricted to the periods during which the difference of temperature between 9 m and the surface exceeds 10 K in the observations (very stable cases, corresponding to 41% of the JJA profiles). Note that profiles of the RRTM-L82–103 (dashed cyan lines), RRTM-K01–103 (dashed green lines) and RRTM-cutoff-103 (dashed purple lines) simulations are almost always perfectly superimposed.
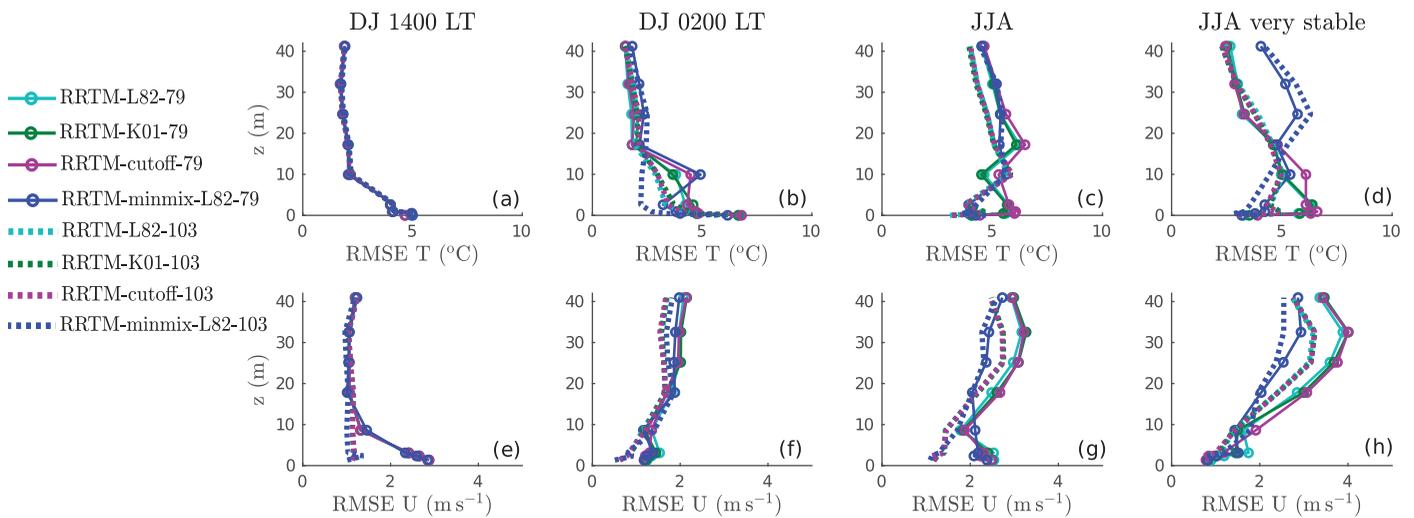
Figure 6. Vertical profiles of the RMSE of the temperature (top plots) and of the wind speed (bottom plots) from LMDZ simulations with respect to observations. The RMSE is calculated at each observation levels after linear interpolation of the simulated profiles to the observation heights. Four composites are shown. Plots a and e show the mean profiles for December–January (DJ) at 1400 LT. Plots b and f show mean profiles for DJ at 0200 LT. Plots c and g show the mean profiles for June–July–August (JJA). Plots d and h show the mean profiles for very stable conditions in JJA, i.e., when the difference of temperature between 9 m and the surface exceeds 10 K in the observations. Note that profiles of the RRTM-L82–103 (dashed cyan lines), RRTM-K01–103 (dashed green lines), and RRTM-cutoff-103 (dashed purple lines) simulations are almost always perfectly superimposed.

the same classes. Note that a similar analysis is made along a 30 m tower over the Ross ice-shelf in Nigro et al. (2017).

Figures 5a and 5d show that DJ convective profiles at 1400 LT are reasonably well represented by LMDZ, in agreement with the 1-D simulations in Vignon et al. (2017b). The RMSEs for temperature and wind speed above 10 m high are about 2.6°C and 1.2 m s^{-1} respectively (Figures 6a and 6e). They increase downward near the surface due to the poor resolution in the surface layer particularly in simulations with the 79 level vertical grid. A cold bias associated to RMSE values around 5°C can be pointed out in all the LMDZ simulations at 1400 LT in DJ. This bias corresponds to a deficit in the net shortwave radiative flux at the surface (not shown). One possible explanation is that LMDZ does not account for daily variations in the albedo, particularly owing to the diurnal cycle of the solar zenith angle (Vignon, 2017). One can further notice that LMDZ simulations better agree with summer observations than ERA-I reanalyses (solid red curves). In particular, the temperature and wind vertical gradients in summertime nocturnal conditions (Figures 5b and 5e) are significantly underestimated in the reanalyses. This is probably due to the use of long-tail functions close to the surface in the turbulent mixing scheme or to an overestimated snow thermal-inertia over ice-sheets in the ECMWF model (Dutra et al., 2015; Sandu et al., 2013). Regardless of the minmix simulations, the representation of the vertical profiles of temperature and wind by LMDZ in summertime and wintertime stable conditions (Figures 5b, 5c, 5e, and 5f) is also reasonable. The increase in vertical resolution (from solid to dashed curves) improves the climatological profiles of temperature and the intersimulation spread. In particular, one can notice the overall decrease in RMSE for both the wind speed and the temperature, especially close to the surface in winter (Figures 6c, 6d, 6g, and 6h) where the vertical gradients are the strongest. In winter, using the minmix configuration (dark blue curves) improves the simulation of the wind speed. However, this configuration significantly degrades the representation of the temperature profiles above 15 m in very stable wintertime conditions even when using the 103 level vertical grid. This is revealed by an underestimation of the convexity of the profiles in the insets in Figure 5c and the RMSE reaches ≈ 6° C at z=25 m (Figure 6d). In Figure 5c, one can further point out the sharp change in the winter vertical gradient of temperature at the first model level ($z \approx 1.4$ m) in the RRTM-minmix-L82–103 simulation (and in a lesser extent in the RRTM-minmix-L82-79). In the RRTM-minmix-L82–103 simulation, as the turbulent mixing of heat in the SBL is stronger than in the surface layer, the temperature at the first model level and the temperature gradient in the surface layer (between the surface and the first-model level) are overestimated. Moreover, the vertical gradient of temperature above the first model level is underestimated, leading to underestimated values of the temperature difference between 9 m (third model level) and the surface (see next section), despite the overestimated inversion in the surface layer.

3.3. Two-Regime Behavior of the Near-Surface Inversion in Clear-Sky Winter Conditions

We now analyze the ability of LMDZ in modeling the SBL regimes. We focus hereafter on clear-sky conditions ($LW_{dn} < 100$ W m^{-2}) in the extended winter (April–September) 2015, when the SBL variability is almost only driven by external mechanical forcings.

Following Vignon et al. (2017a) and van de Wiel et al. (2017), we evidence the two-regime dynamics of the SBL at Dome C by showing the relationship between the near-surface temperature inversion over the first 9 m and the wind speed at 9 m in Figure 7. In the observations (plot a), the relation between the near-surface inversion amplitude and the wind speed takes a characteristic "reversed S-shape" with a "back-folding." The transition between the two branches is particularly abrupt and occurs for wind speeds around 6 m s^{-1}. van de Wiel et al. (2017) show that the lower horizontal branch of the "S" corresponds to a weakly stable regime, in which the surface and the boundary layer are mechanically coupled via turbulence (see also van de Wiel et al., 2012; Van Hooijdonk et al., 2015). The upper horizontal branch corresponds to a very stable regime, in which the strength of the inversion mostly depends on the radiative coupling between the air and the surface and on the diffusive coupling between the snowpack and the surface. The vertical branch corresponds to transitional cases. Figure 7f shows that the ERA-I reanalysis misses the strong inversion values and does not capture the two-regime behavior, pointing to the current failures in the reanalyzed near-surface meteorological fields over the Antarctic Plateau (Dutra et al., 2015).

The other plots show the results for LMDZ simulations. Figures 7b and 7g show the results for LMDZ simulations using the minmix configuration. Interestingly, the comparison with observations is more satisfactory using the 79 level vertical grid (plot b) with in particular stronger near-surface inversions in weak wind speed
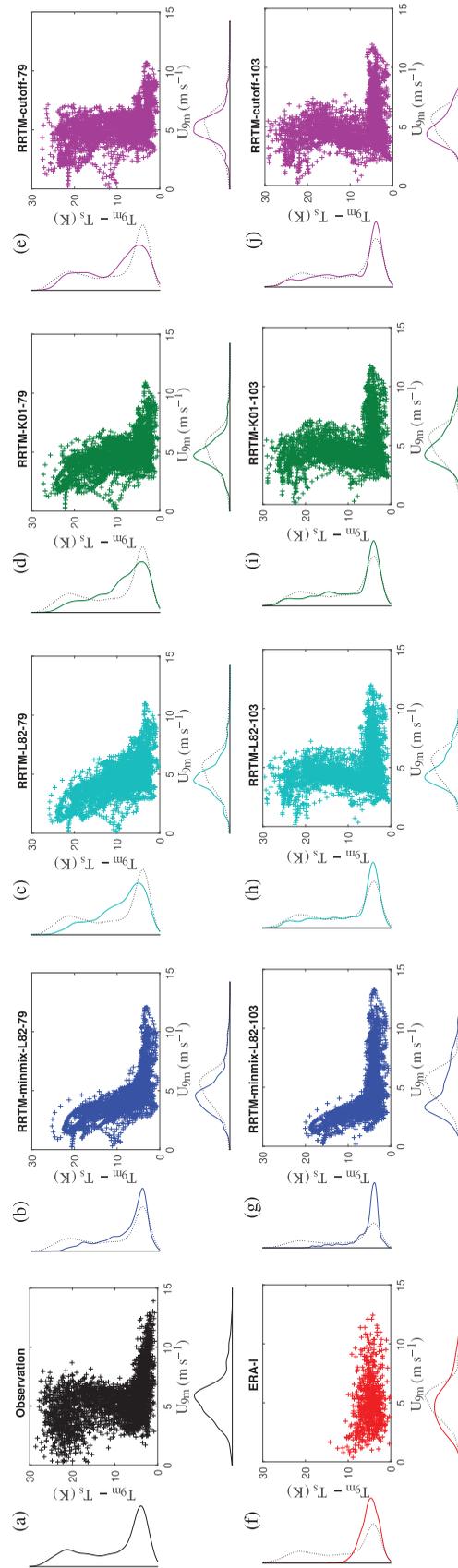
Figure 7. Difference of temperature between 9 m and the surface versus the wind speed at 9 m at Dome C during the clear-sky days in the period 1 April to 30 September 2015 (hourly means). Probability density functions of the wind speed and of the near-temperature inversion are plotted in left and bottom insets and they are superimposed to those of the observations (thin black dotted line). The wind and temperature at $z = 9$ m in model simulations are either the quantities at the third model level (when using the LMDZ 103-level vertical grid) or linear interpolations between quantities at the first and the second model level (when using the LMDZ 79-level vertical grid) or the quantities at the first model level (for ERA-I). Note that the ERA-I data set is restricted to the data at times 0200 LT, 0800 LT, 1400 LT, and 2000 LT.
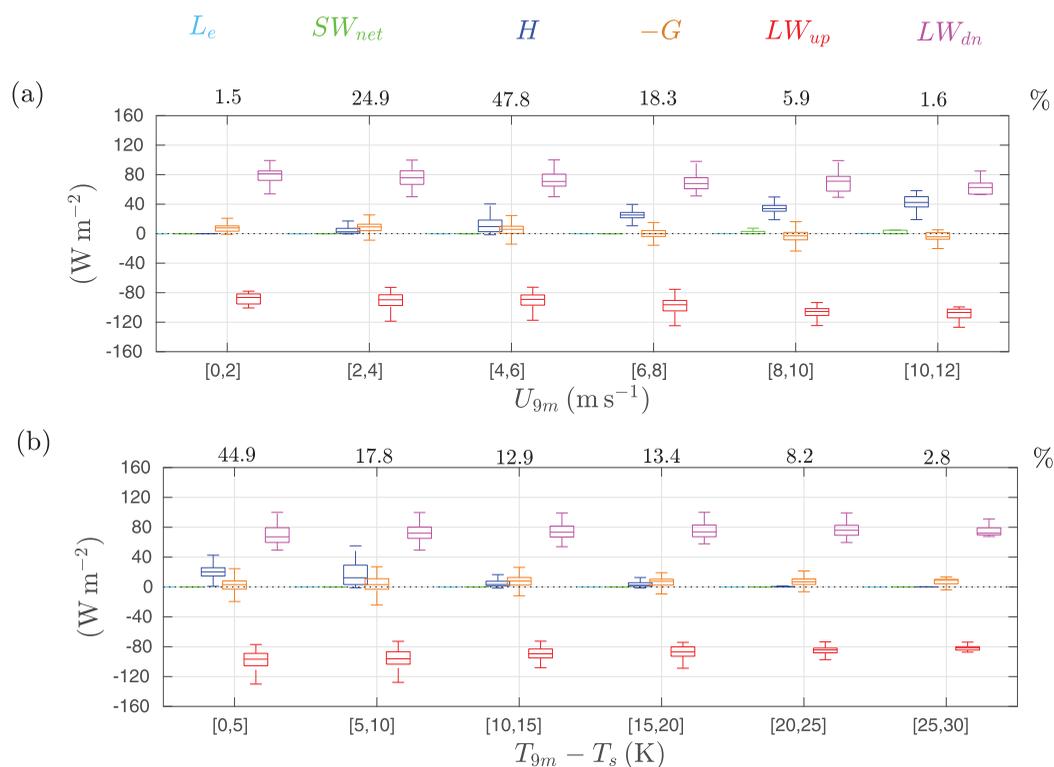
Figure 8. Boxplots of the contributions to the surface energy balance (see Appendix B) for different ranges of U_{9m} (a) or $T_{9m} - T_s$ (b) in the RRTM-K01–103 simulation. The data set is restricted to clear-sky conditions in the period 1 April to 30 September 2015. H is the sensible heat flux, L_e is the latent heat flux, G is the snow heat flux, SW_{net} the net shortwave radiative heat flux, LW_{up} and LW_{dn} the upward and downward longwave radiative fluxes. Fluxes are defined positive downward and in this graph, positive values indicate net fluxes toward the snow surface. Numbers above the plots indicate the percentage of occurrence in each range. Black horizontal dotted lines are the zero lines. In this figure, U_{9m} and T_{9m} are the wind speed and the temperature at the third model level, respectively.

conditions. In fact, using a coarser grid near the surface, the content $T_{9m} - T_s$ is less affected by the enhanced mixing in the turbulence scheme in the boundary layer and is more dependent on the surface layer scheme which is active over a deeper layer (up to the height of the first model level, i.e., $z \approx 6$ m). $T_{9m} - T_s$ thus increases more with decreasing wind speed and reaches larger and more realistic values in Figure 7b compared to plot g. In summary, the minmix configuration tends to alter the representation of SBL regimes in near-surface inversion, and the degradation is even more pronounced when using the 103 level grid.

Figures 7c–7e show that the sharpness of the regime transition in simulations with the 79 level grid depends on the choice of the stability function in the surface layer, in agreement with van de Wiel et al. (2017). In particular, the default long-tail L82 function (Figure 7c) leads to a too smooth transition and too weak near-surface inversion values in weak wind conditions. Results are better when using the K01 functions (Figure 7e) and even better when using the cutoff functions (Figure 7g). However, using cutoff functions in the GCM may not be recommended since it makes the current version of the model crash due to excessive run-away continental surface coolings in free (i.e., without nudging) simulations. For simulations with the 79 level grid, the RRTM-K01–79 configuration is thus a reasonable trade-off for both the representation of the boundary-layer climatology and the representation of SBL regimes at Dome C.

Figures 7h–7j show that when using the refined 103 levels grid, LMDZ also well reproduces the two-regime behavior of the near-surface inversion, with a very sharp transition at $U_{9m} \approx 6$ m s^{-1} and a clear "reversed-S" shaped pattern with a back-folding. It is worth noting that when using the 103 level grid, simulations are less dependent upon the choice of the stability function in the surface layer and no major difference can be identified between the three plots h, i, and j. In fact, with this refined resolution, the

first model layer is shallower. Compared to simulations with the 79 level grid, the Richardon number in the first layer more often falls in an interval where $f_{m,h}$ functions do not significantly depart, i.e., between 0 and 0.1 (see Figure 2).

3.4. Thermodynamical Considerations

We want to assess whether the physical reasons why LMDZ reproduces two regimes of the near-surface inversion are in agreement with previous findings from observations and conceptual models. Figure 8 the magnitude of the different terms of the surface energy balance (see Appendix B for the detailed equation) for different ranges of the wind speed at 9 m (Figure 8a) and for different ranges of the near-surface inversion (Figure 8b) in clear-sky wintertime conditions in the RRTM-K01–103 simulation. One can notice that for $U_{9m} < 4$ m s^{-1} or for $T_{9m} - T_s > 10$ K (i.e., in the very stable regime) the surface sensible heat flux H is null or very close to zero. In this case, the surface energy balance mostly consists in an equilibrium between downward and upward longwave radiation. In its current configuration and using short-tail stability functions for the surface drag coefficient, LMDZ thus reproduces a very stable regime in which the surface is mechanically insulated from the air above, in agreement with theoretical considerations in van de Wiel et al. (2017) or single column simulations in Baas et al. (2017). This result is essentially independent on the vertical resolution (not shown).

Figure 9 shows similar plots as in Figure 8 but for the different contributions to the air enthalpy budget at 9 m (see Appendix B for the detailed equation). One can notice that at high wind speed, there is a quasi balance between heating due to horizontal advection and turbulent cooling due to mixing with the underneath colder surface. Following Mahrt (2017), the role of horizontal advection of heat in strong wind conditions explains why in our simulations, for $U_{9m} > 7$ m s^{-1}, the near-surface inversion no longer
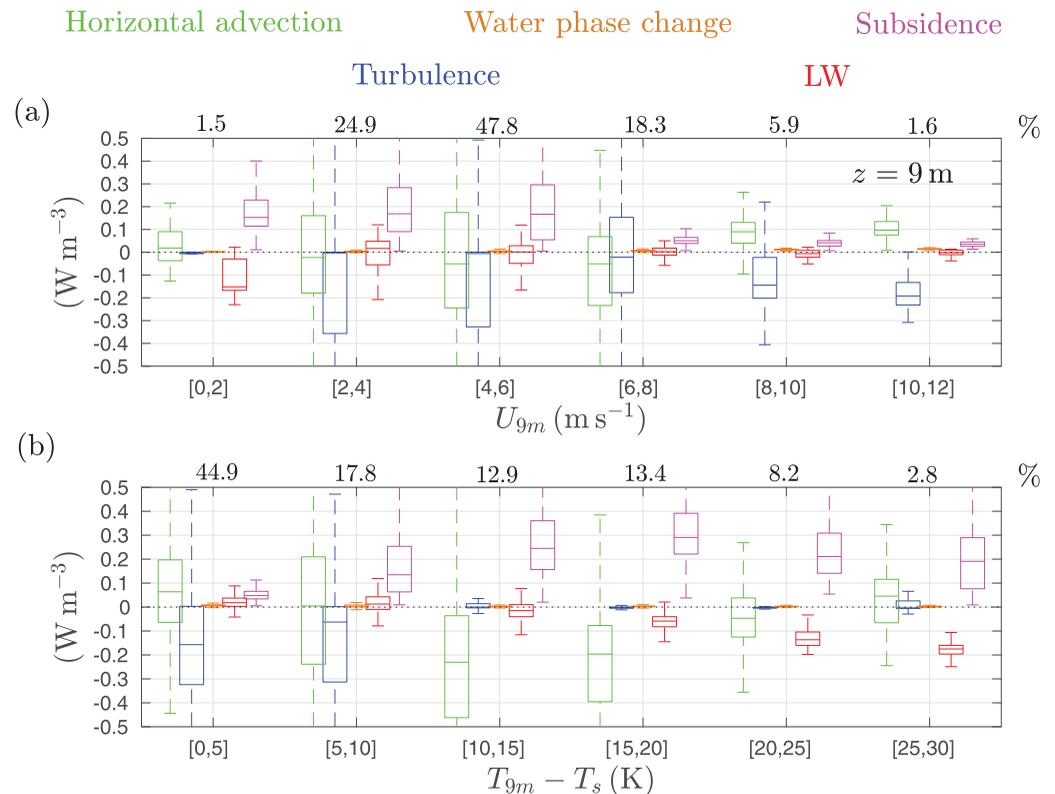
Figure 9. Boxplots of the main contributions to the air enthalpy budget at $z = 9$ m for different ranges of U_{9m} (a) or $T_{9m} - T_s$, (b) in the RRTM-K01–103 simulation. See Appendix B for detailed formulations of each term. The terms associated to the divergence of the shortwave radiative flux and to the nudging are insignificant and are not plotted. The data set is restricted to clear-sky conditions ($LW_{dn} < 100$ W m^{-2}) in the period 1 April to 30 September 2015. Numbers above the plots indicate the percentage of occurrence in each range. Black horizontal dotted lines are the zero lines. In this figure, U_{9m} and T_{9m} are the wind speed and the temperature at the third model level, respectively.

decreases with increasing wind speed—as it would do in a turbulent SBL in horizontally homogeneous conditions—but it stabilizes at values around 3–4 K (see Figures 7e–7h). Moreover, Figure 9b shows that for near-surface inversions greater than 10 K, the enthalpy budget tends to be dominated by the heating associated to the subsidence (adiabatic heating + vertical advection) and by the longwave radiative cooling. This result agrees with the conclusions of van de Berg et al. (2007, 2008) for East-Antarctic domes (in line with other studies like Mirocha and Kosović, 2010 or Edwards, 2009). Our current analysis raises the critical roles of subsidence and longwave cooling in the heat budget of the SBL of polar regions and particularly over the Antarctic Plateau in very stable conditions.

3.5. One Major Sudden Warming Event of the Boundary Layer

Besides the two-regime behavior of the SBL, another critical aspect that should be reproduced by models is the response of the boundary layer to sudden warming events associated to intrusions of air masses from coastal regions. These sudden warming events disrupt the structure of the atmospheric boundary layer and particularly lead to a sudden destruction of the near-surface temperature inversion. Figure 10a depicts the synoptic view of meteorological anomalies during one major warming event that occurred on 7 July 2015. A strong positive anomaly of geopotential at 500 hPa occurs off the Antarctic coast at a longitude of 150°. Note that the 500 hPa level is chosen here because it is the first standard pressure level that does not intersect with the ice-sheet surface. The positive anomaly of geopotential is associated to warm temperature and high moisture anomalies at its west flank due to the advection of lower latitude air toward the Plateau. Figure 10b shows the time evolution of the meteorological fields at Dome C during this event in observations, in the ERA-I reanalyses and in the RRTM-K01–79 simulation.
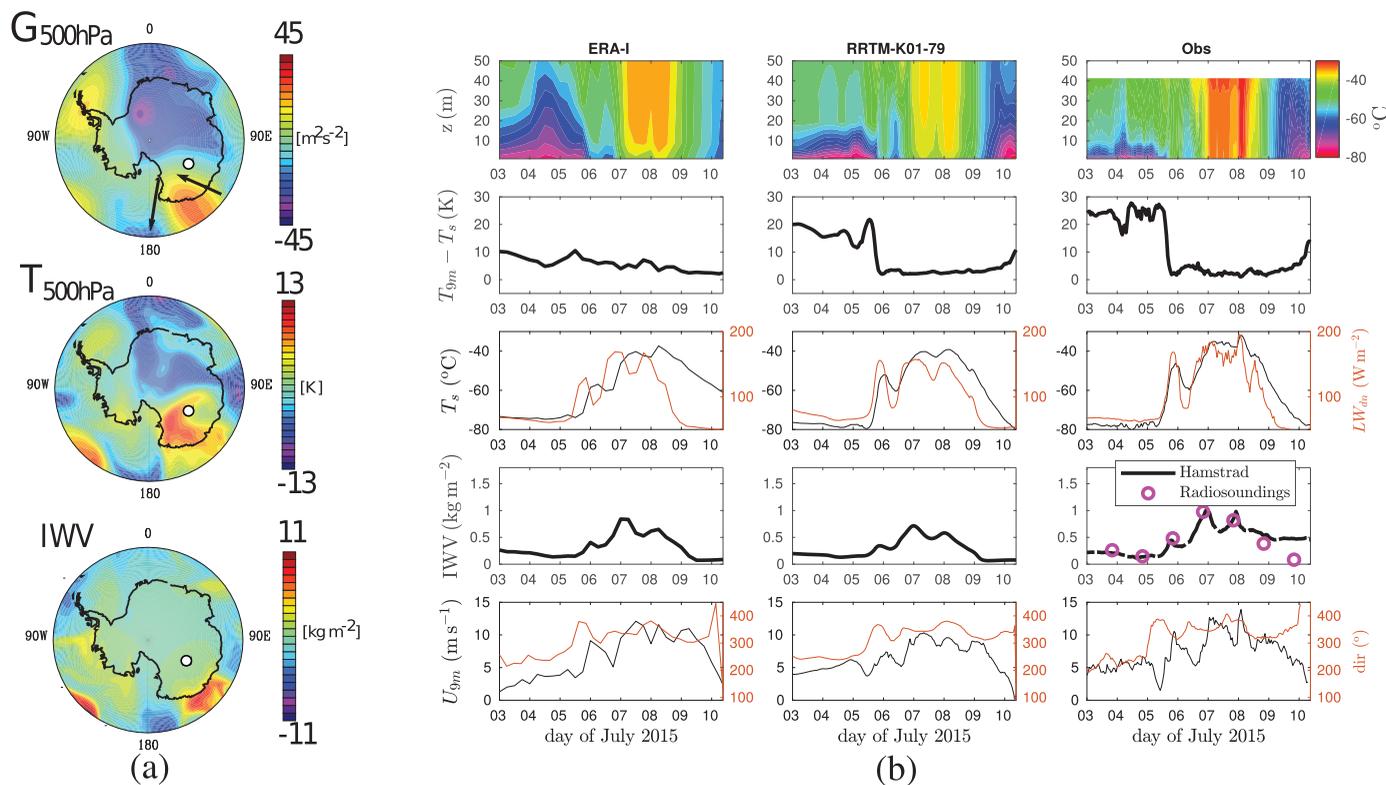
Figure 10. (a) Anomalies of the geopotential at 500 hPa (G$_{500hPa}$), of the temperature at 500 hPa (T$_{500hPa}$), and of the IWV in the ERA-I reanalyses on 7 July, 2015 at 0800 LT with respect to the July climatology over the period 1996–2016. Dome C is indicated with a white dot. (b) Vertical structure of the temperature (first row), time series of the near-surface inversion (second row), time series of T_s and LW_{dn} (third row), time series of the integrated water vapor (fourth row), and time series of the speed and direction of the 9 m wind (fifth row) during one warming event in July 2015 in the ERA-I reanalyses (left plots), in the RRTM-Wmix-79 simulation (middle plots) and in the observations (right plots). In this figure, the wind and temperature at $z = 9$ m in model simulations are either linear interpolations between quantities at the first and the second model level (for the RRTM-Wmix-79 LMDZ simulation) or the quantities at the first model level (for ERA-I).

The observed response of the boundary-layer (right plots) is qualitatively similar to those described for other typical warming events in Gallée and Gorodetskaya (2010) and Genthon et al. (2013). On 4 July, the wind changes from southerly to westerly then northerly direction (fifth row). This change is followed by a top-down warming of the boundary-layer (first row) and to a sharp increase in T_s, LW_{dn} (third row) and IWV (fourth row). Five days later, the surface temperature is back to its initial value.

LMDZ (middle plots) represents correctly the warming event, both in terms of forcing by advection of humidity (dictated by the large-scale nudging) and LW_{dn} at the surface. LMDZ correctly simulates the abrupt warming of the surface from $-80°C$ to $-50°C$ on 5 July, up to $-35°C$ on 7 July, as well as the homogeneously mixed warm temperatures in the first dozens of meters during the following 2 days. Note that the increase in the 10 m wind speed (Gallée & Gorodetskaya, 2010) is due not only to the increase in the wind above the boundary layer but also to the enhanced mixing of momentum and to subsequent deepening of the SBL. The destruction of the near-surface inversion (second row) in the end of 5 July, is well represented in the LMDZ simulation. Indeed, even though the near-surface inversion is slightly underestimated before the warming event in LMDZ (until 5 July), its sharp decrease in the afternoon of 5 July, and the levelling off at a small value (≈ 5 K) during about 4 days is well simulated by the model. This observation can be explained by the sharp change in the LW_{dn} forcing jointly with the sharp increase in the large-scale wind speed (not shown) as well as the advection of warmer air close to the surface. In the ERA-I reanalyses (left plots), the overestimated mixing in stable conditions prevents the occurrence of strong near-surface inversion and subsequently, the inversion destruction due to the warming event is not very marked. Moreover, the surface temperature in the reanalyses decreases too slowly after the warming peak (from 8 to 10 July) probably because of the overestimated value of the snow thermal inertia implemented over the ice-sheet (Dutra et al., 2015).

3.6. Moisture in the Near-Surface Atmosphere

We now assess the modeling of the near-surface moisture at Dome C by LMDZ. Genthon et al. (2017) show that near-surface supersaturation with respect to ice occurs frequently in the SBL at Dome C. While the ERA-I reanalyses allow for such supersaturations despite biases in terms of occurrence and absolute values (Genthon et al., 2017), LMDZ does not allow for supersaturation. This is illustrated in Figure 11a for the RRTM-K01–79 simulation. The relative humidity with respect to ice (RH_i) in LMDZ reaches a ceiling at 100% during a large part of the year, leading to very frequent occurrence of ice-particles in the near-surface atmosphere even when warming events—corresponding to high peaks of LW_{dn}—do not occur (see Figure 11d). In fact, the clouds parametrization of LMDZ condensates as soon as the partial pressure of the vapor exceeds the equilibrium vapor pressure. As in LMDZ, the equilibrium vapor pressure is directly estimated from the Clausius-Clapeyron law, the relative humidity cannot exceed 100%. At temperatures lower than $-15°C$, all the formed cloud hydrometeors are in the ice phase. This explains why LMDZ does not allow for supersaturation with respect to ice and hence why the simulated RH_i is underestimated in periods when supersaturation occurs in the observations.

One can also pointed out that there are periods during which $RH_i < 100\%$ in the observations while the near-surface air is saturated in LMDZ with presence of iced hydrometeors. Note that this observation is very slightly sensitive to the relaxation time of the nudging inside the zoom. Genthon et al. (2017) specify that at temperatures lower than $-60°C$, the time response of the hygrometer increases and thus the reliability of the moisture measurement can be questioned during fast transitions. As the lowest RH_i values are observed at very low temperature (see plot c), this may explain some part of the difference between simulated and observed RH_i. Moreover, although the time series of the specific humidity is reasonably well reproduced (plot b), it is worth noting that at very low temperature, the sensitivity of the near-surface RH_i to both the content in water vapor in the air and to the temperature is high. Subsequently, the value of the relative humidity in the Dome C boundary layer is delicate to simulate since it requires an accurate value of both specific humidity and temperature. However, a further inspection shows that periods when RH_i remains stuck at 100% in LMDZ while it is lower in observations can correspond to both positive and negative near-surface temperature biases (not shown). Underestimating the temperature and subsequently underestimating the equilibrium vapor pressure can thus not be the sole hypothesis to explain the model-observations differences of RH_i when the observed near-surface atmosphere is not saturated. Likewise, the turbulent water flux at the surface is almost always positive (toward the surface) during the extended winter and it cannot be responsible for an excess in water vapor at the first model level when major positive model-
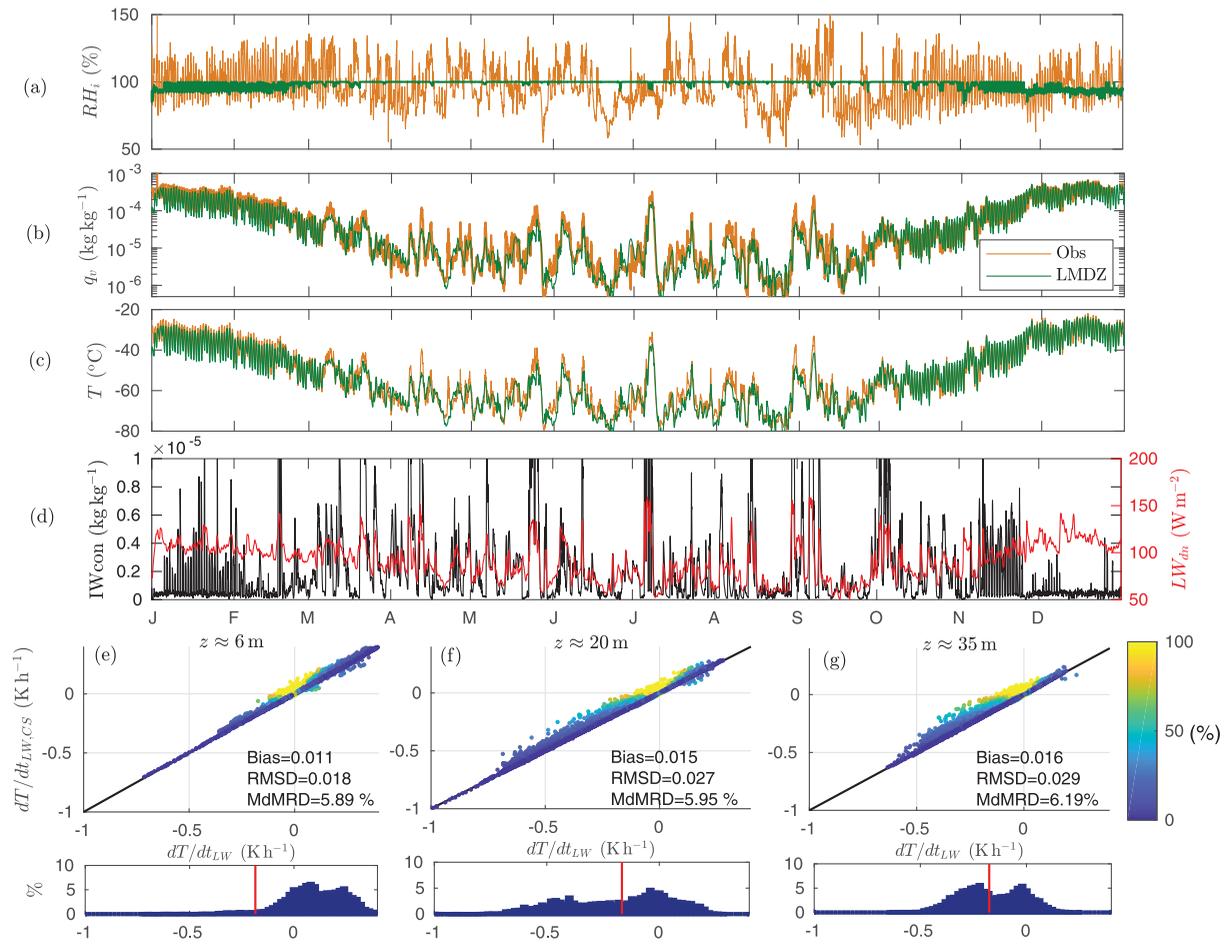
Figure 11. (a–c) 2015 time series of the relative humidity with respect to ice (a), of the specific humidity (b), and of the temperature (c) at 3 m at Dome C in observations and at the first model level ($z \approx 6$ m) in the RRTM-K01–79 LMDZ simulation. (d) 2015 time series of the ice water content (IWcon) at the first model level ($z \approx 6$ m) and of the LW_{dn} flux (red line) in the RRTM-K01–79 LMDZ simulation. (e–g) Scatter plots of the clear-sky component of the air temperature tendency associated with the longwave flux divergence $dT/dt_{LW,CS}$ versus the total tendency dT/dt_{LW} in the RRTM-K01–79 LMDZ simulation (all hourly 2015 data are plotted). Insets show the corresponding distributions (red lines indicates the mean). Plot d refers to the first model level, plot e to the second model level, plot f to the third model level. Black line is the first bissector. Colors show the magnitude of the relative difference $|(d_t T_{LW,CS} - d_t T_{LW})/d_t T_{LW}|$ in %. In the legend, RMSD refers to the Root Mean Square Difference and MdMRD to the Median of the Magnitude of the Relative Difference.

observations differences of RH_i occur. Further investigation is therefore needed to explain the RH_i biases in LMDZ, exploring for instance the sensitivity to the microphysics properties of the ice crystals but this is beyond the scope of the present paper.

We now assess what are the consequences of the excess near-surface condensation in LMDZ simulations on the representation of the boundary-layer dynamics at Dome C. As supersaturation mostly occurs when temperature and specific humidity are low, Genthon et al. (2017) show that they do not significantly affect evaporation/condensation fluxes at the surface. Therefore, supersaturation does not appreciably affect the latent heat flux, already negligible in the surface energy balance at Dome C (King et al., 2001). Moreover, the latent heat released during condensation in the near-surface air is small compared to the other terms of the air energy budget, not only in clear-sky wintertime conditions (Figure 9), but also during the whole year (not shown). The excess condensed water close to the surface in LMDZ might thus modify the boundary-layer dynamics in two different ways. First, it may affect the radiative transfer inside the SBL, and second, it may change the amount of radiative fluxes that reach the surface, modifying the radiative budget of the surface, the surface temperature and subsequently the static stability.

In Figures 11e–11g, we compare the clear-sky component of the longwave radiative temperature tendency $dT/dt_{LW,CS}$ (y axis) with the total tendency dT/dt_{LW} (x axis) at the first three model levels. Note that only the

longwave spectrum is considered since the shortwave tendencies are negligible. One can first notice that the mean difference at the three levels is positive, meaning that iced particles in the atmosphere warm (in average) the near-surface air. The median of the magnitude of the relative difference (MdMRD) ranges between 5% and 6%, indicating that the relative contribution of the hydrometeors to the air radiative heating/cooling is not major but significant. However, large relative differences occur when dT/dt_{LW} is weak (see colors), meaning that the absolute effect of the hydrometeors on the longwave flux divergence in the first tens of meters is moderate (RMSD between 0.018 and 0.029 $K h^{-1}$).

One can then assess the impact of the absence of near-surface supersaturations in LMDZ on the LW_{dn} flux at the surface. We have compared the 2015 time series of LW_{dn} at the surface with that at a height of ≈ 300 m—i.e., at an altitude relatively close to the surface but above the height of the SBL—in the RRTM-K01–79 LMDZ simulation. Only the longwave spectrum is considered here since the impact on the net shortwave fluxes at the surface is negligible compared to the impact on the thermal infrared forcing. The value of the downward longwave radiation at $z=300$ m and that at the surface are very close (mean difference = 0.8 $W m^{-2}$). The root mean square deviation is equal to 2.6 $W m^{-2}$ meaning that the first 300 m of air above the surface contributes (in average) by 2.6 $W m^{-2}$ to the total LW_{dn} flux at the surface. In terms of surface temperature, this corresponds to ≈ 0.9 K for a typical very stable boundary layer in the polar night. This is significant but not critical, especially when the surface is mechanically decoupled from the air above. In LMDZ, the downward longwave radiation that reaches the Dome C surface thus mostly depends on the atmospheric properties above the SBL. Hence, the absence of supersaturation and the subsequent excess of water condensation in the first 300 m above the surface (and thus in the SBL) do not strongly affect the radiative budget at the surface and the surface temperature in the model.

Even though the absence of moisture supersaturations in the boundary layer in LMDZ is a critical issue for the modeling of moist processes above the ice-sheet, its impact on the representation of the boundary layer dynamics remains moderate. However, the failure of the cloud parametrization upper in the troposphere and the lack or excess of hydrometeors over the whole atmospheric column may be responsible for substantial biases in the LW_{dn} flux at the surface. Excess condensation could lead to positive biases in surface temperature as those observed in section 3.1 with significant consequences on the SBL structure.

4. Climate Simulations With the Free LMDZ Model: Impact of the Turbulent Mixing Parametrization Over the Antarctic Ice-Sheet

One may wonder whether the calibration of the model at Dome C affects the near-surface meteorological fields at the continental scale. In particular, we have shown that removing the artificial mixing thresholds in the turbulent mixing parametrization and using short-tail stability functions in the surface layer improves the representation of the SBL regime transition and of strong near-surface temperature inversions. Hereafter, we show an analysis of the specific effect of the turbulent mixing parametrization on the surface temperature and on the near-surface wind over the whole Antarctic continent. This analysis is similar to that in King et al. (2001) but it further benefits from the previous "calibration phase" at Dome C and from direct comparison with in situ observations. We consider 10 year climate free (not nudged) simulations with the standard $144 \times 142 \times 79$ regular grid of the model. The first simulation has been run with the recommended RRTM-K01–79 configuration, i.e., with no mixing thresholds in the turbulence scheme and with short tail stability functions in the surface layer. The second simulation has been run with the RRTM-minmix-L82-79 configuration, with enhanced mixing formulations in both the boundary layer and the surface layer. Figure 12a shows that the wintertime near-surface inversion over the Antarctic ice-sheet is significantly reduced with the RRTM-minmix-L82-79 configuration compared to RRTM-K01–79 as expected by the enhanced turbulent mixing in the former configuration. Moreover, Figure 12c shows that the RRTM-minmix-L82-79 simulation is significantly warmer at the surface compared to the RRTM-K01–79 simulation (by 3.9°C in average over the ice-sheet). This is particularly noticeable in winter at Dome C (plot b). The downward radiative fluxes at the surface in both simulations are similar (difference less than 0.8 $W m^{-2}$ for both the shortwave and longwave downward radiative fluxes). In fact, the surface temperature difference is mostly due to the larger (in magnitude) sensible heat flux in the RRTM-minmix-L82-79 simulation: 19.61 $W m^{-2}$ in average over the ice-sheet in RRTM-minmix-L82-79 instead of 15.58 $W m^{-2}$ in RRTM-K01–79. This observation is in agreement with the conclusions on the stretched-grid and nudged simulations in section 3.1.
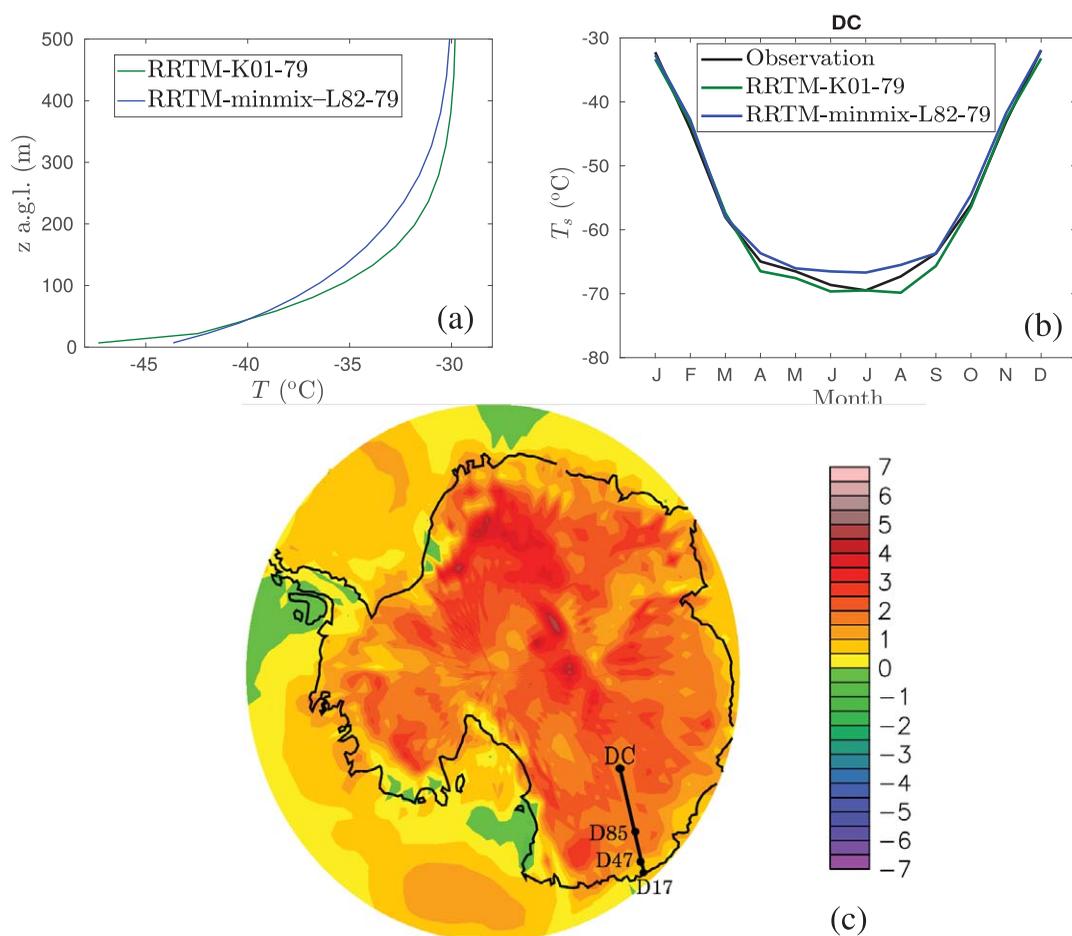
Figure 12. (a) Vertical profiles of the temperature (JJA mean) averaged over the Antarctic ice-sheet in the free LMDZ simulations. (b) Time series of the monthly mean surface temperature in the free LMDZ simulations and in observations at Dome C (DC). In this plot, we have used all the available surface temperature data from observations in the period 2011–2015. (c) Difference of yearly mean surface temperature (in °C) over Antarctica in free LMDZ simulations between the RRTM-minmix-L82-79 and the RRTM-K01–79 configurations. The black straight line is the transect in Adélie Land along which the meteorological stations Dome C (DC), D85, D47, and D17 are set-up.

Figure 13 shows the winter averaged vertical profiles of the two components of the wind, averaged over the whole ice-sheet. It emphasizes the different vertical distributions of momentum, with on average deeper mixing and weaker wind speed in the RRTM-minmix-L82-79 simulation. In agreement with King et al. (2001), using a turbulent scheme that allows for sharp decrease of the turbulent mixing with increasing stability thus leads to an overall increase of the wind speed in the first hundreds of meters above the ice-sheet, especially at the peak level. The increase in the wind speed is not limited to the coastal regions, but it extends toward the escarpment regions and even over a large part of the Plateau (not shown). In LMDZ simulations, the choice of the turbulent mixing parametrization thus affects the circulation at the continental scale.

Furthermore, the wind field very close to the surface remains not very satisfying in the free LMDZ simulations. Indeed, Figure 14 compares the monthly mean wind speed at the standard 10 m near-surface level with observations at four Antarctic automatic weather stations along a Plateau-Coast transect in Adélie Land (black straight line in Figure 12c). Extrapolation to observation levels are also plotted (dotted line, see legend for details). Further information on measurements at D17, D47, and D85 stations can be found in Wendler et al. (1993), Barral et al. (2014), and Amory et al. (2017) (see also the webpage http://amrc.ssec.wisc.edu/aws/index.php?region=Adelie\%20Coast&year=2017&mode=uw). Note that while landscapes at Dome C, D47, and D85 are relatively homogeneous—suggesting a representativity of the local measurement at the LMDZ grid scale ($\approx$ 110 km $\times$ 140 km)—the topographic and geographic spatial variability near D17 at the 10 km scale makes the simulation-observation comparison delicate at this site. Figure 14b should thus be interpreted with caution.
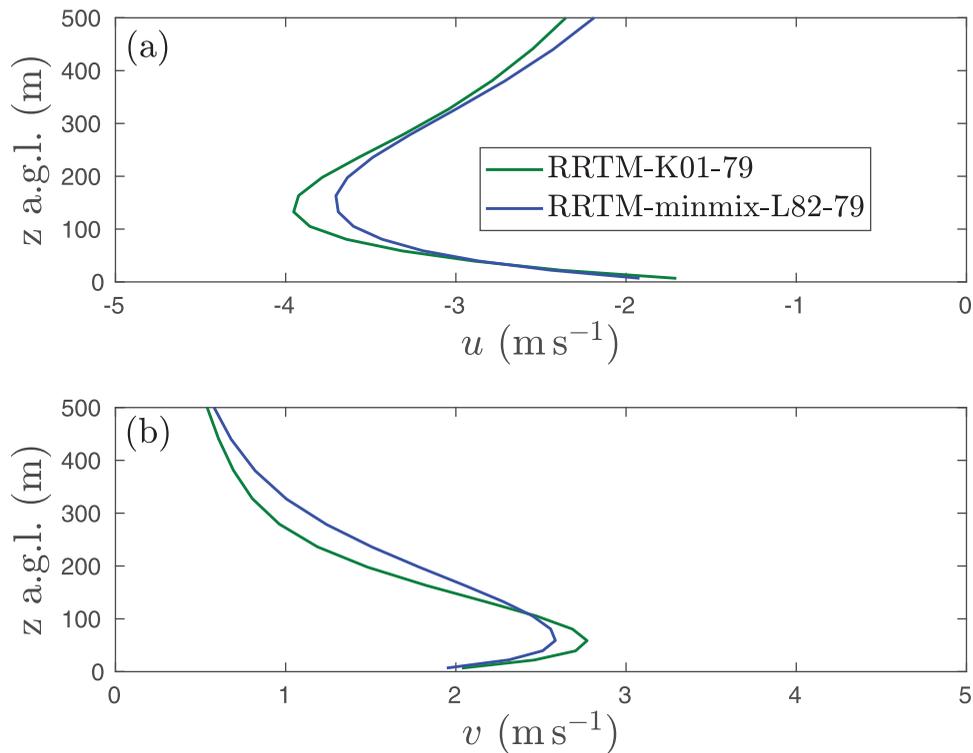
Figure 13. (a) June–July–August mean near-surface vertical profiles of the zonal and (b) of the meridional components of the wind, averaged over the whole Antarctic ice-sheet.

One can point out an underestimation of the wind speed at three Antarctic stations compared to observations. Largest differences with observations occur at D47 station, in a region of strong katabatic winds. By mass conservation at the continental scale, underestimating the flow toward the ocean in the periphery of the continent could explain an underestimation of the overall drainage flow at low levels over the whole Antarctic continent (James, 1989). It is worth noting that biases are similar for the RRTM-K01–79 (green lines) and RRTM-minmix-L82–79 (blue lines) simulations suggesting that the turbulence parametrization is not the main cause. The hydrostatic hypothesis of the LMDZ model can be hardly suspected since nonhydrostatic effects tend to weaken the flow at lower levels in the katabatic layer (Cassano & Parish, 2000). One could otherwise suspect issues related to biases in the continental-scale circulation like an underestimation of the climatological trough off the Antarctic coasts leading to underestimated ocean-ice-sheet pressure gradients, one of the drivers of the coastal Antarctic winds (Van den Broeke et al., 2002; Van den Broeke & Van Lipzig, 2003). However, comparison of the 500 hPa geopotential between the free LMDZ simulations and ERA-I has not revealed significant underestimation of the geopotential off Adélie Land. One could also question the vertical resolution, that can be too coarse in the katabatic region where sharp and shallow wind jets frequently occur. Moreover, the continental-scale smoothening out of the topography inherent to the use of coarse horizontal resolutions in GCMs could lead to an underestimation of the local slopes in the escarpment and coastal regions of the ice-sheet, where strong local katabatic flows are generated.

Another hypothesis to explain the near-surface wind speed underestimation is the absence of a blowing snow parametrization in the model. Kodama et al. (1985) estimate that the positive feedbacks of the blowing snow on the speed of the flow (sublimation effect and density effect due to the presence of solid particles in the air) could be responsible for a significant enhancement of the speed of the wind. However, Gosink (1989) further found that the impact of blowing snow on the katabatic wind speeds is significant only for wind speeds higher than ≈ 28 m s^{-1}. In addition, Lenaerts and van den Broeke (2012) found no appreciably effect of the drifting snow on the wind speed in simulations with a regional climate model, but their model does not account for the mass of solid snow particles in the flow. It is thus still unclear whether neglecting blowing snow could lead to a large underestimation of the wind speed in katabatic regions.
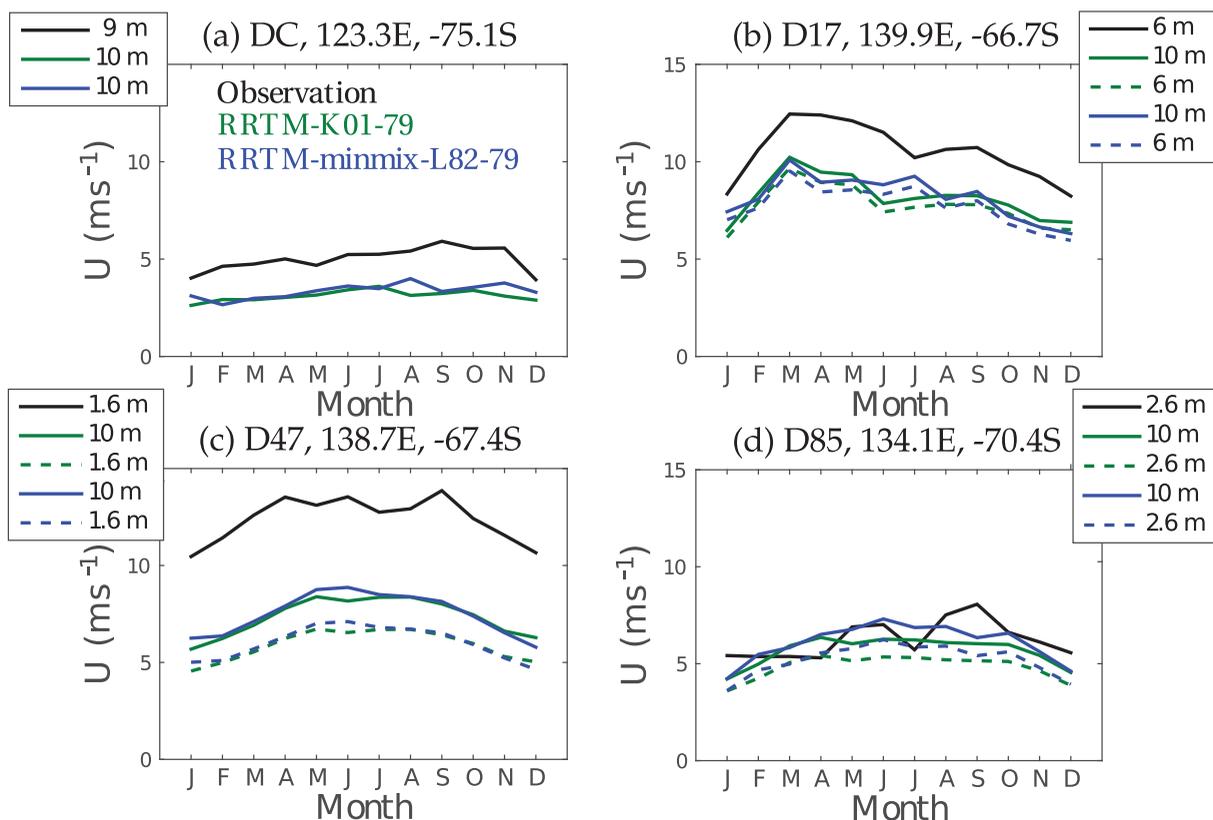
Figure 14. Comparison of the monthly mean wind speed in LMDZ simulations with that observed at four stations on a Plateau-coast transect (Dome C: plot a, D17: plot b, D47: plot c, D85: plot d). For each station, the simulated 10 m wind speed is plotted. In plots b–d, as the observation height z is well lower than 10 m, an approximated value of the simulated wind speed at z is calculated with the relation $U(z) = U(10\,\text{m})\ln(z/z_0)/\ln(10/z_0)$, where $z_0 = 1$ mm the roughness length value prescribed over ice-sheets in LMDZ. Such logarithmic extrapolation - based on the Monin-Obukhov similarity theory—is acceptable because the surface layer at D17, D47, and D85 is most of the time statically neutral (Amory et al., 2017; Barral et al., 2014). All the available observational data at Dome C and D17 (respectively, D47 and D85) in the period 2011–2015 (respectively, 2010–2014) have been used to make this plot. Note that the height of the instruments is not constant and it can change significantly within one year due to snow accumulation/erosion. Stations D17, D47, and D85 are leveled at the reference height once a year.

Future studies on the evaluation of the large-scale Antarctic circulation and on the representation of the Antarctic coastal flows in LMDZ should be addressed in the future, assessing the sensitivity to the turbulence scheme, to the model resolution and eventually to the inclusion of a blowing-snow parametrization.

5. Conclusions

In the present work, we assess the ability of the state-of-the-art version of the LMDZ GCM in modeling the dynamics of the boundary layer over the Antarctic Plateau. The model is first run with a stretched-grid over Dome C, with a strong nudging outside the zoom region and a very weak nudging inside. This configuration enables to well constrain the synoptic circulation with reanalyses, leaving the whole physical package of LMDZ working over the Antarctic Plateau. Then, the model is run in a free configuration with its standard grid to assess the impact of the turbulent mixing parametrization over the whole Antarctic continent. Our analysis has led to the following conclusions.

1. First, the implementation of the RRTM radiative scheme leads to a significant improvement of the simulated LW_{dn} and surface temperature at Dome C. The remaining surface temperature biases in the simulations are correlated with biases in LW_{dn}, raising the critical need of a correct modeling of the longwave radiative transfer in the particularly cold and dry conditions over the Antarctic Plateau to obtain satisfactory surface temperatures over the ice-sheet. The remaining LW_{dn} biases could be either due to a failure

of the RRTM scheme in clear-sky Antarctic condition or to an excess (or misrepresentation) of cloud hydrometeors above Dome C.

2. Climatological near-surface vertical profiles of temperature and wind speed at Dome C are reasonably well reproduced by LMDZ except the profiles of temperature in very stable conditions when using the minmix configuration.

3. Unlike ERA-I, the physical package in LMDZ enables the representation of two distinct SBL regimes in clear-sky wintertime conditions at Dome C. However, the representation of strong near-surface inversions and of the regime transition is degraded when using enhanced mixing formulations in the SBL. Using short-tail stability functions in the surface layer enables sharper and more realistic regime transitions with the standard 79 level vertical grid of the model. Subsequently, using short-tail stability functions is thus preferable for Antarctic simulations. The characteristic "reversed-S" shaped dependency of the near-surface inversion with the wind speed is even better reproduced when using the 103 level vertical grid.

4. In clear-sky wintertime conditions, when the boundary layer is very stable, the surface energy balance almost reduces to an equilibrium between the upward and downward longwave fluxes. The air heat budget close to the surface is mostly governed by a longwave radiative cooling and a warming associated to large-scale subsidence.

5. Sudden warming events of the boundary layer associated to northerly advections of warm and moist air and the associated near-surface inversion destruction are reasonably well reproduced by the nudged LMDZ. Therefore, if the free model correctly represents the oceanic air intrusions into the Antarctic continent, the response of the boundary layer over the Plateau should be in principle well simulated.

6. LMDZ does not account for near-surface supersaturation with respect to ice. This phenomenon, though critical for the representation of moist processes over the ice-sheet, has a moderate impact on the structure of the boundary layer in the model. However, this conclusion only stands for humidity biases inside the boundary layer, not for the whole atmospheric column above Dome C. Likely excess condensation higher in the troposphere might have a significant impact on the LW_{dn} flux and on the surface temperature.

7. In agreement with King et al. (2001), analysis of a free LMDZ simulation with the recommended configuration without enhanced mixing formulations in both the boundary layer and the surface layer shows a strengthening of the continental-scale temperature inversion and a cooling of the surface in winter compared to simulations with enhanced mixing in stable conditions. However, an underestimation of the near-surface wind speed is present in our free simulations and its origin has not been clearly identified so far.

Persisting biases in the LW_{dn} flux at the surface have not been explained. In addition to the inability of LMDZ to model ice-supersaturations and to correctly simulate the near-surface relative humidity, this invites to an in depth evaluation of the radiative transfer and of the cloud parametrization in the model over Antarctica. Last but not least, even though the present study shows a reasonable agreement between simulations and observations in terms of temperature and wind field structures in the boundary layer, a further investigation of the physical processes in very stable conditions at Dome C remains to be carried out. Additional observing systems measuring the radiative vertical divergence (Hoch et al., 2007) for instance or fine scale modeling studies using large eddy simulations or even direct numerical simulations could be valuable. Furthermore, Vignon et al. (2017b) as well as the present study evidenced that a correct modeling of the SBL over the Antarctic Plateau requires the removal of artificially enhanced turbulence formulations. However, this may be problematic over other continents, in regions where sub-grid mixing processes not included in classical parametrizations of turbulence actually participate to the subgrid mixing (e.g., mesoscale motions or internal waves). Alternative approaches like the implementation of an additional small-scale gravity wave drag (Steeneveld et al., 2008; Tsiringakis et al., 2017) have been proposed. A study is currently underway in LMDZ.

Appendix A: Tropospheric State Above Dome C in Simulations With a Stretched-Grid and Nudging

A satisfying representation of the boundary layer by the model first requires a correct modeling of the synoptic fields above Dome C. Even in case when LMDZ is nudged with reanalyses, we want to ascertain whether the overall climatology of the troposphere above Dome C is correctly reproduced. Note that given simulations are nudged with temperature, wind and moisture, the tropospheric profiles of the three quantities in LMDZ are very close to those in ERA-I except of course in the boundary layer. Figure A1a compares
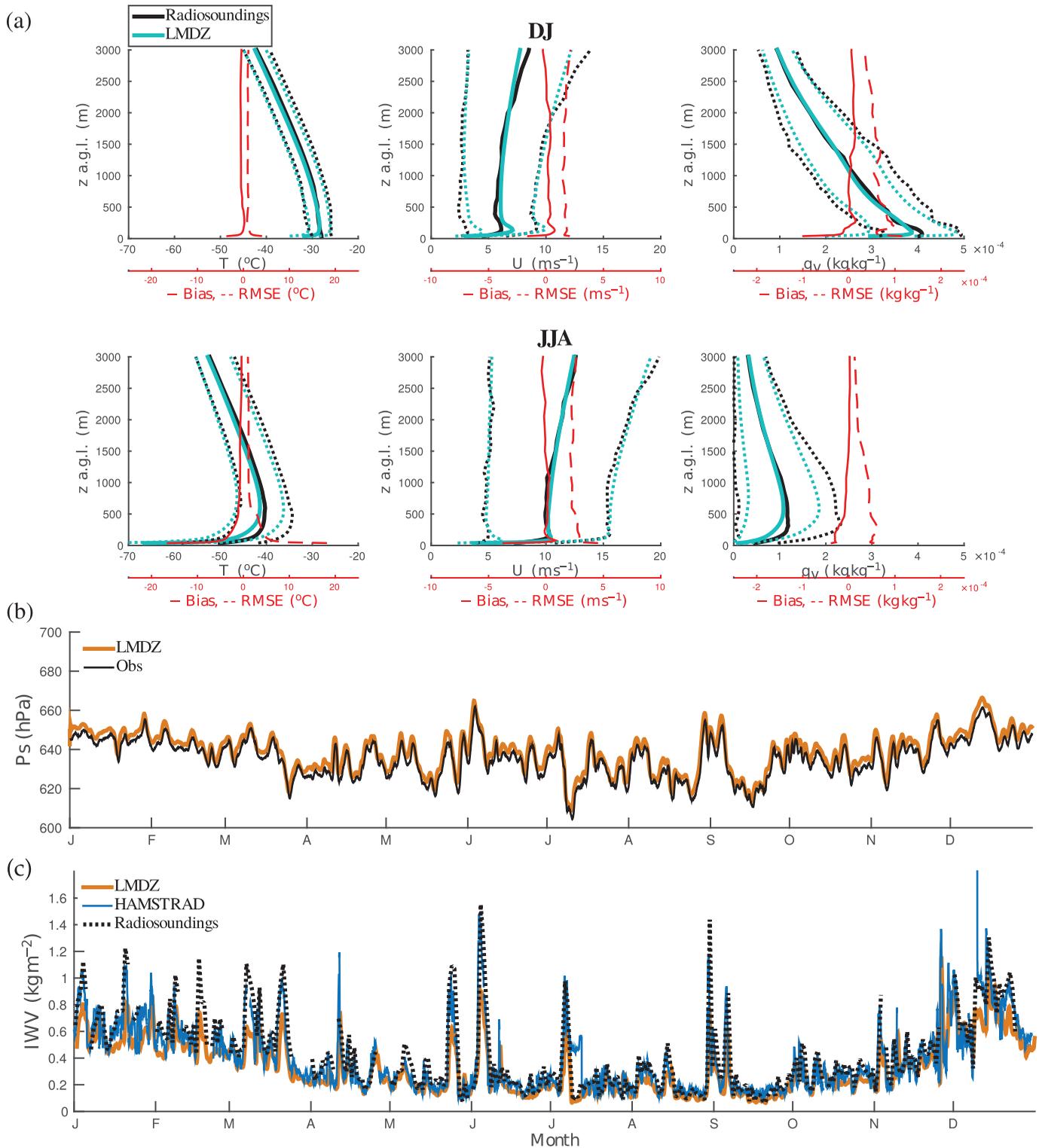
Figure A1. (a) 2015 profiles of the temperature T, the wind speed U, and the specific humidity q_v from the radiosoundings (solid black lines) and in the RRTM-K01–79 LMDZ simulation (solid blue line) $\pm$one standard deviation (dotted lines). The model outputs data set is restricted to hourly means at 2000 LT (1200 UTC) i.e. the time at which radiosoundings are launched. Upper row shows DJ means, lower row shows the JJA mean. Dotted lines show $\pm$one standard deviation. Red lines shows LMDZ biases and RMSE with respect to the radiosoundings. (b) 2015 time seres of the surface pressure at Dome C in observations and in the RRTM-K01–79 LMDZ simulation. (c) 2015 time series of the integrated water vapor in the RRTM-K01–79 LMDZ simulation, from HAMSTRAD measurements and from radiosoundings.

LMDZ (RRTM-K01–79 simulation) and radiosounding profiles of temperature, wind speed, and specific humidity in the trophoperic column above Dome C during the two most contrasted seasons: in summer (December–January mean, left column) and in winter (June–July–August mean, right column). The model output data set is restricted to data at 2000 LT (1200 UTC, time of radiosounding launches) to make a proper comparison. All plots show a reasonable agreement between model and observations. Not only the mean profiles (solid lines) but also the spread (standard deviations, dotted lines) are correctly reproduced. However, major biases and RMSE (red lines) are found for temperature and specific humidity in the first 500 m in winter. This result is surprising since the winter climatological profiles of temperature over the first 45 m in the RRTM-K01–79 simulation show a reasonable agreement with tower observations on the Dome C tower (Figure 5). When the Antarctic surface-based temperature inversion is strong, i.e., in winter, near-surface radiosoundings measurements can be affected by large thermal lag errors up to an altitude of about 250 m above the surface (Mahesh et al., 1997). Without correction algorithms, it is hard to disentangle model deficiencies from measurement errors. Instead of applying such algorithms, we prefer using tower measurements rather than radiosoundings to evaluate the simulations close to the surface.

Figure A1b shows that the evolution of the time series of the surface pressure (Ps) agrees with observations. The slight offset of about 3 hPa in the simulation is due to the fact that the mesh encompassing Dome C has a mean altitude lower by 33 m than the summit of the dome. The IWV is also in reasonable agreement with observations (Figure A1c) even though one can point out an underestimation of the "peaks" associated to significant advections of warm and moist air from coastal regions.

The key message here is that the overall large-scale meteorological fields are well reproduced in the nudged-simulation and this ensures that the dynamical forcings on the atmospheric boundary layer are correct. This makes us confident that the differences between model simulations and observations that can be evidenced in the first dozens of meters above the surface are primarily related to physical parametrizations and/or vertical resolution rather than consequences of deficiencies in the modeling of synoptic fields. However, the IWV values during warming events should be considered with caution.

Appendix B: Surface Energy Balance and Air Heat Budget Equation

B1. Surface Energy Balance
Defining fluxes positive downward, the surface energy balance reads:

$$SW_{dn}+LW_{dn}+SW_{up}+LW_{up}+H+L_e-G=0 \tag{B1}$$

where H is the sensible heat flux, L_e is the latent heat flux, G is the ground heat flux, SW_{dn} and LW_{dn} are the downward shortwave and longwave fluxes, respectively. SW_{up} and LW_{up} are the upward shortwave and longwave radiative fluxes, respectively, and these terms are always negative.

B2. Air Heat Budget Equation
The heat budget equation of the air in our LMDZ simulations reads (Holton, 1992; van de Berg et al., 2007):

$$\rho c_p \partial_t T = \underbrace{-\rho c_p(u\partial_x T + v\partial_y T)}_{\text{Horizontal Advection}} \underbrace{-\rho c_p w\partial_z T + \omega}_{\text{Subsidence}}$$
$$\underbrace{-\partial_z SW}_{\text{SW}} \underbrace{-\partial_z LW}_{\text{LW}} \underbrace{-\partial_z(THF)}_{\text{Turbulence}} + \underbrace{\mathcal{J}}_{\text{Water Phase change}} + \underbrace{\mathcal{N}}_{\text{nudging}} \tag{B2}$$

where w is the vertical velocity, c_p is the isobaric heat capacity per unit mass of dry air, ρ the air density, LW is the longwave radiative flux, SW is the shortwave radiative flux, THF the turbulent heat flux, J is the diabatic heating rate per unit volume due to water phase changes and $\mathcal{N}$ the nudging term. Here, we assume $\omega=d P/dt \approx -\rho gw$ (Holton, 1992) where P is the pressure and g is the magnitude of gravity.

References

Agosta, C., Favier, V., Krinner, G., Gallée, H., & Genthon, C. (2013). High resolution modelling of the Antarctic surface mass balance, application for the twentieth, twenty first and twenty second centuries. *Climate Dynamics*, *41*, 3247–3260. https://doi.org/10.1007/s00382-013-1903-9

Amory, C., Gallée, H., Naaim-Bouvet, F., Favier, V., Vignon, E., Picard, G., . . . Bellot, H. (2017). Seasonal variations in drag coefficients over a sastrugi-covered snowfield of coastal East Antarctica. *Boundary-Layer Meteorology*, *164*(1), 107–133. https://doi.org/10.1007/s10546-017-0242-5

Argentini, S., Pietroni, I., Mastrantonio, G., Viola, A. P., Dargaud, G., & Petenko, I. (2014). Observations of near surface wind speed, temperature and radiative budget at Dome C, Antarctic Plateau during 2005. *Antarctic Science*, *26*, 104–112. https://doi.org/10.1017/S0954102013000382

Aristidi, E., Agabi, K., Azouit, M., Fossat, E., Vernin, J., Travouillon, T., . . . Walden, V. (2005). An analysis of temperatures and wind speeds above Dome C, Antarctica. *Astronomy and Astrophysics*, *430*, 739–746. https://doi.org/10.1051/0004-6361:20041876

Baas, P., van de Wiel, B. J. H., van der Linden, S. J. A., & Bosveld, F. C. (2017). From near-neutral to strongly stratified: adequately modelling the nocturnal boundary layer at Cabauw. *Boundary-Layer Meteorology*, https://doi.org/10.1007/s10546-017-0304-8

Barral, H., Genthon, C., Trouvilliez, A., Brun, C., & Amory, C. (2014). Blowing snow at D17, Adélie Land, Antarctica: Atmospheric moisture issues. *The Cryosphere*, *8*, 1905–1919. https://doi.org/10.5194/tc-8-1905-2014

Bazile, E., Couvreux, F., Moigne, P., Genthon, L. C., Holtslag, A. A. M., & Svensson, G. (2014). GABLS4: An intercomparison case to study the stable boundary layer over the Antarctic Plateau, *GEWEX News*, *24*(4).

Bazile, E., Couvreux, F., Moigne, P. L., & Genthon, C. (2015). First workshop on the GABLS4 experiment, *GEWEX News*, *25*(3).

Berkelhammer, M., Noone, D. C., Steen-Larsen, H. C., Bailey, A., Cox, C. J., O'neill, M. S., . . . White, J. W. C. (2016). Surface-atmosphere decoupling limits accumulation at summit, Greenland. *Science Advances*, *2*(4). https://doi.org/10.1126/sciadv.1501704

Bintanja, R., van der Linden, E. C., & Hazeleger, W. (2012). Boundary layer stability and arctic climate change: A feedback study using ec-earth. *Climate Dynamics*, *39*(11), 2659–2673. https://doi.org/10.1007/s00382-011-1272-1

Bromwich, D. H., Nicolas, J. P., Monaghan, A. J., Lazzara, M. A., Keller, L. M., Weidner, G. A., & Wilson, A. B. (2013a). Central West Antarctica among the most rapidly warming regions on Earth. *Nature Geoscience*, *6*, 139–145. https://doi.org/10.1038/ngeo1671

Bromwich, D. H., Otieno, F. O., Hines, K. M., Manning, K. W., & Shilo, E. (2013b). Comprehensive evaluation of polar weather research and forecasting model performance in the Antarctic. *Journal of Geophysical Research: Atmospheres*, *118*, 274–292. https://doi.org/10.1029/2012JD018139

Casasanta, G., Pietroni, I., Petenko, I., & Argentini, S. (2014). Observed and modelled convective mixing-layer height at Dome C, Antarctica. *Boundary-Layer Meteorology*, *151*, 587–608. https://doi.org/10.1007/s10546-014-9907-5

Cassano, J. J., Nigro, M. A., & Lazzara, M. A. (2016). Characteristics of the near-surface atmosphere over the Ross ice shelf, Antarctica. *Journal of Geophysical Research: Atmospheres*, *121*, 3339–3362. https://doi.org/10.1002/2015JD024383

Cassano, J. J., & Parish, T. R. (2000). An analysis of the nonhydrostatic dynamics in numerically simulated Antarctic katabatic flows. *Journal of Atmospheric Science*, *57*(6), 891–898. https://doi.org/10.1175/1520-0469(2000)057<0891:AAOTND>2.0.CO;2

Cassano, J. J., Parish, T. R., & King, J. C. (2001). Evaluation of turbulent surface flux parameterizations for the stable surface layer over Halley, Antarctica. *Monthly Weather Review*, *129*, 26–46.

Cerni, T. A., & Parish, T. R. (1984). A radiative model of the stable nocturnal boundary layer with application to the polar night. *Journal of Applied Meteorology and Climatology*, *23*, 1563–1572.

Coindreau, O., Hourdin, F., Haeffelin, M., Mathieu, A., & Rio, C. (2007). Assessment of physical parametrizations using a global climate model with stretchable grid and nudging. *Monthly Weather Review*, *135*, 1474–1490. https://doi.org/10.1175/MWR3338.1

Cosme, E., Hourdin, F., Genthon, C., & Martinerie, P. (2005). Origin of dimethylsulfide, non-sea-salt sulfate, and methanesulfonic acid in eastern Antarctica. *Journal of Geophysical Research*, *110*, D03302. https://doi.org/10.1029/2004JD004881

Cuxart, J., Holtslag, A. A. M., Beare, R. J., Bazile, E., Beljaars, A., Cheng, A., . . . Xu, K.-M. (2006). Single-column model intercomparison for a stably stratified atmospheric boundary layer. *Boundary-Layer Meteorology*, *118*(2), 273–303. https://doi.org/10.1007/s10546-005-3780-1

Deleersnijder, E. (1992). *Modélisation hydrodynamique tridimensionnelle de la circulation générale estivale de la région du détroit de bering* (in French, Ph.D. thesis). Faculté des sciences appliquées, Université Catholique de Louvain.

Derbyshire, S. H. (1999). Boundary-layer decoupling over cold surfaces as a physical boundary-instability. *Boundary-Layer Meteorology*, *90*, 297–325.

Dufresne, J.-L., Foujols, M.-A., Denvil, S., Caubel, A., Marti, O., Aumont, O., . . . Vuichard, N. (2013). Climate change projections using the IPSL-CM5 earth system model: From CMIP3 to CMIP5. *Climate Dynamics*, *40*(9), 2123–2165. https://doi.org/10.1007/s00382-012-1636-1

Dutra, E., Sandu, Balsamo, I., Beljaars, G., Freville, A., Vignon, H. E., & Brun, E. (2015). *Understanding the ECMWF winter surface temperature biases over Antarctica* (Tech. Memo. 762). Reading, UK: European Center for Medium range Weather Forecast.

Edwards, J. M. (2009). Radiative processes in the stable boundary layer: Part ii: The development of the nocturnal boundary layer. *Boundary-Layer Meteorology*, *131*(2), 127–146. https://doi.org/10.1007/s10546-009-9363-9

England, D. E., & McNider, R. T. (1995). Stability functions based upon shear functions. *Boundary-Layer Meteorology*, *74*, 113–130.

Freville, H., Brun, E., Picard, G., Tatarinova, N., Arnaud, L., Lanconelli, C., . . . van den Broeke, M. (2014). Using MODIS land surface temperatures and the Crocus snow model to understand the warm bias of ERA-Interim reanalyses at the surface in Antarctica. *The Cryosphere*, *8*, 1361–1373. https://doi.org/10.5194/tc-8-1361-2014

Gallée, H., Barral, H., Vignon, E., & Genthon, C. (2015). A case study of a low level jet during OPALE. *Atmospheric Chemistry and Physics*, *15*, 6237–6246. https://doi.org/10.5194/acp-15-1-2015

Gallée, H., & Gorodetskaya, I. (2010). Validation of a limited area model over Dome C, Antarctic Plateau, during winter. *Climate Dynamics*, *23*, 61–72. https://doi.org/10.1007/s00382-008-0499-y

Genthon, C., & Krinner, G. (1998). Convergence and disposal of energy and moisture on the Antarctic polar cap from ECMWF reanalyses and forecasts. *Journal of Climate*, *11*, 1703–1716.

Genthon, C., Piard, L., Vignon, E., Madeleine, J.-B., Casado, M., & Gallée, H. (2017). Atmospheric moisture supersaturation in the near-surface atmosphere at Dome C, Antarctic Plateau. *Atmospheric Chemistry and Physics*, *17*, 1–14. https://doi.org/10.5194/acp-17-1-2017

Genthon, C., Six, D., Gallée, H., Grigioni, P., & Pellegrini, A. (2013). Two years of atmospheric boundary layer observations on a 45-m tower at Dome C on the Antarctic Plateau. *Journal of Geophysical Research: Atmospheres*, *118*, 3218–3232. https://doi.org/10.1002/jgrd.50128

Genthon, C., Six, D., Scarchilli, C., Ciardini, V., & Frezzotti, M. (2015). Meteorological and snow accumulation gradients across Dome C, East Antarctic plateau. *International Journal of Climatology*, *36*, 455–466. https://doi.org/10.1002/joc.4362

Genthon, C., Town, M. S., Six, D., Favier, V., Argentini, S., & Pellegrini, A. (2010). Meteorological atmospheric boundary layer measurements and ECMWF analyses during summer at Dome C, Antarctica. *Journal of Geophysical Research*, *115*, D05104. https://doi.org/10.1029/2009JD012741

Gosink, J. P. (1989). The extension of a density current model of katabatic winds to include the effects of blowing snow and sublimation. *Boundary-Layer Meteorology*, *49*, 367–394.

Grenfell, T. C., & Warren, S. G. (1994). Reflection of solar radiation by the Antarctic snow surface at ultraviolet, visible, and near-infrared wavelengths. *Journal of Geophysical Research*, *99*, 18,669–18–684.

Hoch, S. W., Calanca, P., Philipona, R., & Ohmura, A. (2007). Year-round observation of longwave radiative flux divergence in Greenland. *Journal of Applied Meteorology*, *46*, 1469–1479. https://doi.org/10.1175/JAM2542.1

Holton, J. R. (1992). *An Introduction to Dynamic Meteorology*. San Diego, CA: Academic Press.

Hourdin, F. (1992). *Etude et simulation numérique de la circulation générale des atmosphéres planétaires* (in French, Ph.D. thesis). Paris, France: Laboratoire de Météorologie Dynamique.

Hourdin, F., Couvreaux, F., & Menut, L. (2002). Parameterization of the dry convective boundary layer based on a mass flux representation of thermals. *Journal of Atmospheric Science*, *59*, 1105–1123.

Hourdin, F., Grandpeix, J.-Y., Rio, C., Bony, S., Jam, A., Cheruy, F., . . . Roehrig, R. (2013). LMDZ5B: The atmospheric component of the IPSL climate model with revisited parameterizations for clouds and convection. *Climate Dynamics*, *40*(9), 2193–2222. https://doi.org/10.1007/s00382-012-1343-y

Hourdin, F., Mauritsen, T., Gettelman, A., Golaz, J.-C., Balaji, V., Duan, Q., . . . Williamson, D. (2017). The art and science of climate model tuning. *Bulletin of the American Meteorological Society*, *98*(3), 589–602. https://doi.org/10.1175/BAMS-D-15-00135.1

Hudson, S., & Brandt, R. E. (2005). A look at the surface based temperature inversion on the Antarctic Plateau. *Journal of Climate*, *118*, 1673–1696.

Iacono, M. J., Mlawer, E. J., CLough, S. A., & Morcrette, J. J. (2000). Final technical report for the project: Application of improves radiation modeling to general circulation models. *Journal of Geophysical Research*, *105*, 14,873–14,890.

James, I. M. (1989). The Antarctic drainage flow: Implications for hemispheric flow on the southern hemisphere. *Antarctic Science*, *1*, 279–290.

King, J. C., & Connolley, W. M. (1997). Validation of the surface energy balance over the Antarctic Ice Sheet in the U.K. Meteorological Office unified climate model. *Journal of Climate*, *10*, 1273–1287.

King, J. C., Connolley, W. M., & Derbyshire, S. H. (2001). Sensitivity of modelled Antarctic climate to surface and boundary-layer flux parametrizations. *Quarterly Journal of the Royal Meteorological Society*, *127*, 779–794.

Kodama, Y., Wendler, G., & Gosink, J. (1985). The effect of blowing snow on katabatic winds in Antarctica. *Annals of Glaciology*, *6*, 59–62.

Krinner, G., Largeron, C., Ménégoz, M., Agosta, C., & Brutel-Vuilmet, C. (2014). Oceanic forcing of Antarctic climate change: A study using a stretched-grid atmospheric general circulation model. *Journal of Climate*, *27*, 5786–5800. https://doi.org/10.1175/JCLI-D-13-00367.1

Krinner, G., Magand, O., Simmonds, I., Genthon, C., & Dufresne, J.-L. (2007). Simulated Antarctic precipitation and surface mass balance at the end of the 20th and 21st centuries. *Climate Dynamics*, *28*, 215–230. https://doi.org/10.1007/s00382-006-0177-x

Krinner, G., Viovy, N., de Noblet-Ducoudré, N., Ogée, J., Polcher, J., Friedlingstein, P., . . . Prentice, I. C. (2005). A dynamic global vegetation model for studies of the coupled atmosphere-biosphere system. *Global Biogeochemical Cycles*, *19*, GB1015. https://doi.org/10.1029/2003GB002199

Lanconelli, C., Busetto, M., Dutton, E. G., Knig-Langlo, G., Maturilli, M., Sieger, R., . . . Yamanouchi, T. (2011). Polar baseline surface radiation measurements during the international polar year 2007–2009. *Earth System Science Data Discussions*, *3*, 1–8. https://doi.org/10.5194/essd-3-1-2011

Lenaerts, J. T. M., & van den Broeke, M. R. (2012). Modeling drifting snow in Antarctica with a regional climate model: 2. Results. *Journal of Geophysical Research: Atmospheres*, *117*, D05109. https://doi.org/10.1029/2010JD015419

Libois, Q., Picard, G., Arnaud, L., Morin, S., & Brun, E. (2014). Modeling the impact of snow drift on the decameter-scale variability of snow properties on the Antarctic Plateau. *Journal of Geophysical Research: Atmospheres*, *119*, 662–681. https://doi.org/10.1002/2014JD022361

Louis, J. F., Tiedtke, M., & Geleyn, J.-F. (1982). *A short history of the operational PBL parametrization at ECMWF*. Paper presented at the ECMWF workshop on boundary layer parametrization, ECMWF, Reading.

Mahesh, A., Walden, V. P., & Warren, S. G. (1997). Radiosonde temperature measurements in strong inversions: Correction for thermal lag based on an experiment at the South Pole. *Journal of Atmospheric and Oceanic Technology*, *14*(1), 45–53. https://doi.org/10.1175/1520-0426(1997)014<0045:RTMISI>2.0.CO;2

Mahrt, L. (2017). Heat flux in the strong-wind nocturnal boundary layer. *Boundary-Layer Meteorology*, *163*, 161–177. https://doi.org/10.1007/s10546-016-0219-9

McNider, R. T., Steeneveld, G. J., Holtslag, A. A. M., Pielke, R. A., Mackaro, S., Pour-Biazar, A., . . . Christy, J. (2012). Response and sensitivity of the nocturnal boundary layer over land to added longwave radiative forcing. *Journal of Geophysical Research: Atmospheres*, *117*, D14106. https://doi.org/10.1029/2012JD017578

Mirocha, J. D., & Kosović, B. (2010). A large-eddy simulation study of the influence of subsidence on the stably stratified atmospheric boundary layer. *Boundary-Layer Meteorology*, *134*(1), 1. https://doi.org/10.1007/s10546-009-9449-4

Mlawer, E. J., Taubman, S. J., Brown, P. D., Iacono, M. J., & Clough, S. A. (1997). Radiative transfer for inhomogeneous atmospheres: RRTM, a validated correlated-k model for the longwave. *Journal of Geophysical Research*, *102*, 16,663–16,682.

Monahan, A. H., Rees, T., He, Y., & McFarlane, N. (2015). Multiple regimes of wind, stratification, and turbulence in the stable boundary layer. *Journal of the Atmospheric Sciences*, *72*, 3178–3198. https://doi.org/10.1175/JAS-D-14-0311.1

Morcrette, J.-J. (1991). Radiation and cloud radiative properties in the European Center for Medium Range and Forecasts forecasting system. *Journal of Geophysical Research*, *96*, 9121–9132.

Morcrette, J.-J., Mlawer, E. J., Iacono, M. J., & Clough, S. A. (2001). Impact of the radiation-transfer scheme RRTM in the ECMWF forecasting system, *ECMWF Newsletter*, *91*, 2–9.

Nicolas, J. P., & Bromwich, D. H. (2014). New reconstruction of Antarctic near-surface temperatures: Multidecadal trends and reliability of global reanalyses. *Journal of Climate*, *27*(21), 8070–8093. https://doi.org/10.1175/JCLI-D-13-00733.1

Nigro, M. A., Cassano, J. J., Wille, J., Bromwich, D. H., & Lazzara, M. A. (2017). A self-organizing-map-based evaluation of the Antarctic mesoscale prediction system using observations from a 30-m instrumented tower on the Ross Ice Shelf, Antarctica. *Weather and Forecasting*, *32*(1), 223–242. https://doi.org/10.1175/WAF-D-16-0084.1

Palchetti, L., Bianchini, G., Natale, G. D., & Guasta, M. D. (2015). Far-infrared radiative properties of water vapor and clouds in Antarctica. *Bulletin of the American Meteorological Society*, *96*(9), 1505–1518. https://doi.org/10.1175/BAMS-D-13-00286.1

Petenko, I., Argentini, S., Pietroni, I., Viola, A., Mastrantonio, G., Casasanta, G., . . . Bondoux, E. (2014). Observations of optically active turbulence in the planetary boundary layer by Sodar at the Concordia astronomical observatory, Dome C, Antarctica. *Astronomy and Astrophysics*, *568*(A44). https://doi.org/10.1051/0004-6361/201323299

Pietroni, I., Argentini, S., Petenko, I., & Sozzi, R. (2012). Measurements and parametrizations of the atmospheric boundary-layer height at Dome C, Antarctica. *Boundary-Layer Meteorology*, *143*, 189–206. https://doi.org/10.1007/s10546-011-9675-4

Previdi, M., Smith, K. L., & Polvani, L. M. (2013). The Antarctic atmospheric energy budget. Part I: climatology and intraseasonal-to-interannual variability. *Journal of Climate*, *26*, 6406–6414. https://doi.org/10.1175/JCLI-D-12-00640.1

Ricaud, P., Bazile, E., del Guasta, M., Lanconelli, C., Grigioni, P., & Mahjoub, A. (2017). Genesis of diamond dust, ice fog and thick cloud episodes observed and modelled above dome c, Antarctica. *Atmospheric Chemistry and Physics*, *17*(8), 5221–5237. https://doi.org/10.5194/acp-17-5221-2017

Ricaud, P., Genthon, C., Durand, P., Attié, J., Carminati, F., Canut, G., . . . Rose, T. (2012). Summer to winter diurnal variabilities of temperature and water vapour in the lowermost troposphere as observed by HAMSTRAD over Dome C, Antarctica. *Boundary-Layer Meteorology*, *143*, 227–259.

Ricaud, P., Grigioni, P., Zbinden, R., Attié, J.-L., Genoni, L., Galeandro, A., . . . Legovini, P. (2015). Review of tropospheric temperature, absolute humidity and integrated water vapour from the HAMSTRAD radiometer installed at Dome C, Antarctica, 2009–14. *Antarctic Science*, *27*, 598–616. https://doi.org/10.1017/S0954102015000334

Rio, C., Hourdin, F., Couvreux, F., & Jam, A. (2010). Resolved versus parametrized boundary-layer plumes. Part II: continuous formulations of mixing rates for mass-flux schemes. *Boundary-Layer Meteorology*, *135*(3), 469–483. https://doi.org/10.1007/s10546-010-9478.

Riordan, A. J. (1977). Variations of temperature and air motion in the 0- to 32-meter layer at Plateau Station, Antarctica, In P. C. Dalrymple, et al. (Eds.), *Meteorological Studies at Plateau Station, Antarctica, Antarctic Research Series* (Vol. 25, pp. 113–127), Washington, DC: American Geophysical Union. https;//doi/doi: 10.1002/9781118664872.ch8

Sandu, I., Beljaars, A., Bechtold, P., Mauritsen, T., & Balsamo, G. (2013). Why is it so difficult to represent stably stratified conditions in numerical weather prediction (nwp) models. *Journal of Advances in Modeling Earth Systems*, *5*, 117–133. https://doi.org/10.1002/jame.20013

Skamarock, W. C., Klemp, J. B., Dudhia, J., Gill, D. O., Barker, D. M., Duda, M. G., . . . Powers, J. G. (2008). *A description of the advanced research WRF version 3* (113 p.). Boulder, CO: Mesoscale and Microscale Meteorology Division, National Center for Atmospheric Research (NCAR). Retrieved from http://www2.mmm.ucar.edu/wrf/users/doc/arw_v3.pdf

Smith, K. L., & Polvani, L. M. (2017). Spatial patterns of recent Antarctic surface temperature trends and the importance of natural variability: lessons from multiple reconstructions and the cmip5 models. *Climate Dynamics*, *48*(7), 2653–2670. https://doi.org/10.1007/s00382-016-3230-4

Steeneveld, G. J., Holtslag, A. A. M., Nappo, C. J., van de Wiel, B. J. H., & Mahrt, L. (2008). Exploring the possible role of small-scale terrain drag on stable boundary layers over land. *Journal of Applied Meteorology and Climatology*, *47*(10), 2518–2530. https://doi.org/10.1175/2008JAMC1816.1

Steig, E. J., Schneider, D. P., Rutherford, S. D., Mann, M. M., Comiso, J. C., & Shindell, D. T. (2009). Warming of the Antarctic ice-sheet surface since the 1957 international geophysical year. *Nature*, *457*, 459–462.

Sterk, H. A. M., Steeneveld, G. J., & Holtslag, A. M. M. (2013). The role of snow-surface coupling, radiation, and turbulent mixing in modeling a stable boundary layer over arctic sea ice. *Journal of Geophysical Research: Atmospheres*, *118*, 1199–1217. https://doi.org/10.1002/jgrd.50158

Svensson, G., Holtslag, A. A. M., Kumar, V., Mauritsen, T., Steeneveld, G. J., Angevine, W. M., . . . Zampieri, M. (2011). Evaluation of the diurnal cycle in the atmospheric boundary layer over land as represented by a variety of single-column models: The second GABLS experiment. *Boundary-Layer Meteorology*, *140*(2), 177–206. https://doi.org/10.1007/s10546-011-9611-7

Tomasi, C., Petkov, B., Benedetti, E., Vitale, V., Pellegrini, A., Dargaud, G., . . . Valenziano, L. (2006). Characterization of the atmospheric temperature and moisture conditions above Dome C (Antarctica) during austral summer and fall months. *Journal of Geophysical Research*, *111*, D20305. https://doi.org/10.1029/2005JD006976

Tomasi, C., Petkov, B., Benedetti, E., Valenziano, L., & Vitale, V. (2011). Analysis of a 4 year radiosonde data set at Dome C for characterizing temperature and moisture conditions of the Antarctic atmosphere. *Journal of Geophysical Research: Atmospheres*, *116*, D15304. https://doi.org/10.1029/2011JD015803

Tsiringakis, A., Steeneveld, G.-J., & Holtslag, A. A. M. (2017). Small-scale orographic gravity wave drag in stable boundary layers and its impact on synoptic systems and near surface meteorology. *Quarterly Journal of the Royal Meteorological Society*, *143*(704), 1504–1516. https://doi.org/10.1002/qj.3021

Turner, J., Lachlan-Cope, T. A., Colwell, S., Marshall, G. J., & Connolley, W. M. (2006). Significant warming of the Antarctic winter troposphere. *Science*, *311*, 914–1917. https://doi.org/10.1126/science.1121652

Turner, J., Lu, H., White, I., King, J. C., Phillips, T., Hosking, J. S., . . . Deb, P. (2016). Absence of 21st century warming on Antarctic Peninsula consistent with natural variability. *Nature*, *535*, 411–415. https://doi.org/10.1038/nature18645

van de Berg, W. J., van den Broeke, M. R., & van Meijgaard, E. (2007). Heat budget of the East Antarctic lower atmosphere derived from a regional atmospheric climate model. *Journal of Geophysical Research: Atmospheres*, *112*, D23101. https://doi.org/10.1029/2007JD008613.

van de Berg, W. J., van den Broeke, M. R., & van Meijgaard, E. (2008). Spatial structures in the heat budget of the Antarctic atmospheric boundary layer. *The Cryosphere*, *2*(1), 1–12. https://doi.org/10.5194/tc-2-1-2008

van de Wiel, B. J. H., Moene, A. F., Jonker, H. J. J., Baas, P., Basu, S., Donda, J. M. M., . . . Holtslag, A. A. M. (2012). The minimum wind speed for sustainable turbulence in the nocturnal boundary layer. *Journal of Atmospheric Science*, *69*, 3097–3115. https://doi.org/10.1175/JAS-D-12-064.1

van de Wiel, B. J. H., Vignon, E., Baas, P., van Hooijdonk, I. G. S., van der Linden, S. J. A., van Hooft, J. A., . . . Genthon, C. (2017). Regime transition in near-surface temperature inversions: A conceptual model. *Journal of Atmospheric Science*, *74*, 1057–1073. https://doi.org/10.1175/JAS-D-16-0180.1

Van den Broeke, M., & Van Lipzig, N. P. M. (2003). Factors controlling the near-surface wind field in Antarctica. *Monthly Weather Review*, *21*(9), 1417–1431.

Van den Broeke, M. R., Lipzig, N. P. M. V., & Meijgaard, E. V. (2002). Momentum budget of the East Antarctic atmospheric boundary layer: Results of a regional climate model. *Journal of the Atmospheric Sciences*, *59*(21), 3117–3129. https://doi.org/10.1175/1520-0469(2002)059<3117:MBOTEA>2.0.CO;2

van der Linden, S. J. A., Baas, P., van Hooft, J. A., van Hooijdonk, I. G. S., Bosveld, F., & van de Wiel, B. J. H. (2017). Local characteristics of the nocturnal boundary layer in response to external pressure forcing. *Journal of Applied Meteorology and Climatology*, *56*(11), 3035–3047. https://doi.org/10.1175/JAMC-D-17-0011.1

Van Hooijdonk, I. G. S., Donda, J. M. M., Clercx, H. J. H., Bosveld, F. C., & van de Wiel, B. J. H. (2015). Shear capacity as prognostic for nocturnal boundary layer regimes. *Journal of the Atmospheric Sciences*, *72*, 1518–1532. https://doi.org/10.1175/JAS-D-14-0311.1

Van Hooijdonk, I. G. S., Moene, A. F., Scheffer, M., Clercx, H. J. H., & Van de Wiel, B. J. H. (2017). Early warning signals for regime transition in the stable boundary layer: A model study, *Boundary-Layer Meteorology*, *162*(2), 283–306. https://doi.org/10.1007/s10546-016-0199-9

Vignon, E. (2017). *The extreme atmospheric boundary layer over the Antarctic Plateau and its representation in climate models*. (PhD thesis). Grenoble, France: Université Grenoble Alpes.

Vignon, E., Genthon, C., Barral, H., Amory, C., Picard, G., Gallée, H., . . . Argentini, S. (2016). Momentum and heat flux parametrization at Dome C, Antarctica: A sensitivity study. *Boundary-Layer Meteorology*, *162*(2), 341–367. https://doi.org/10.1007/s10546-016-0192-3

Vignon, E., van de Wiel, B. J. H., van Hooijdonk, I. G. S., Genthon, C., van der Linden, S. J. A., van Hooft, J. A., . . . Casasanta, G. (2017a). Stable boundary layer regimes at Dome C, Antarctica: Observation and analysis. *Quarterly Journal of the Royal Meteorological Society*, *143*(704), 1241–1253. https://doi.org/10.1002/qj.2998

Vignon, E., Hourdin, F., Genthon, C., Gallée, H., Bazile, E., Lefebvre, M.-P., . . . Van de Wiel, B. J. H. (2017b). Antarctic boundary layer parametrization in a general circulation model: 1-D simulations facing summer observations at Dome C. *Journal of Geophysical Research: Atmospheres*, *122*, 6818–6843. https://doi.org/10.1002/2017JD026802

Walters, J. T., McNider, R. T., Shi, X., Norris, W. B., & Christy, J. R. (2007). Positive surface temperature feedback in the stable nocturnal boundary layer. *Geophysical Research Letters*, *34*, L12709. https://doi.org/10.1029/2007GL029505.

Wendler, G., André, J. C., Pettré, P., Gosink, J., & Parish, T. (1993). Katabatic winds in Adélie coast. In D. H. Bromwich & C. R. Stearns (Eds.), *Antarctica Meteorology and Climatology: Studies Based on Automatic Weather Stations*. Washington, DC: American Geophysical Union. https://doi.org/10.1029/AR061p0023

Wild, M., Ohmura, A., Gilden, H., Morcrette, J. J., & Slingo, A. (2001). Evaluation of downward longwave radiation in general circulation models. *Journal of Climate*, *14*, 3227–3239.

Wille, J. D., D. H., Bromwich, M. A., Nigro, J. J., Cassano, M. M., M. A., Lazzara, S.-H. & Wang, (2016). Evaluation of the amps boundary layer simulations on the ross ice shelf with tower observations. *Journal of Applied Meteorology and Climatology*, *55*(11), 2349–2367. https://doi.org/10.1175/JAMC-D-16-0032.1

Yamada, T. (1983). Simulations of nocturnal drainage flows by a q^2l turbulence closure model. *Journal of the Atmospheric Sciences*, *40*, 91–106.